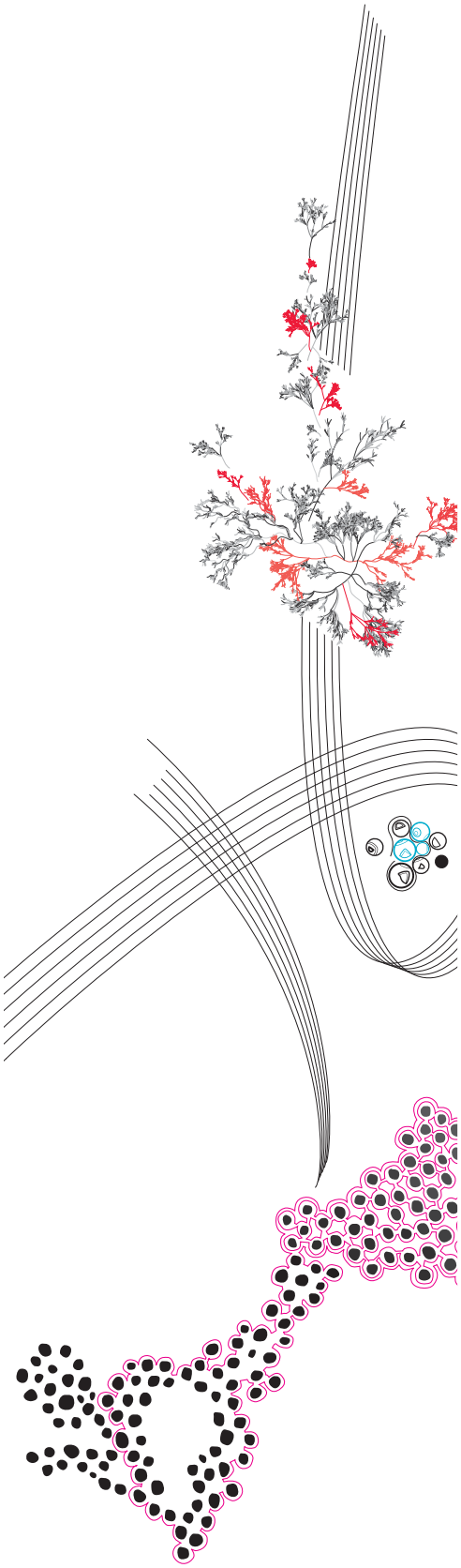

MSc Thesis Applied Mathematics

Numerical continuation schemes for 1D patterns in neural fields

Wouter Gerrit van Harten

Supervisor:
dr. H.G.E. Meijer

Graduation committee :
prof.dr. C. Brune
dr. H.G.E. Meijer
dr. M. Schlottbom

October 2021

Department of Applied Mathematics
Faculty of Electrical Engineering,
Mathematics and Computer Science

UNIVERSITY OF TWENTE.

Contents

1 Introduction

Understanding the inner workings of our brain has been of great interest for years and could, for example, lead towards better treatment of cognition and diseases, e.g. spreading depression. Brain imaging in a variety of regions of the brain has shown that complex activity patterns can emerge in neuronal tissue [19, 25, 27, 34, 35].

At the mesoscale level of neural populations, it is appropriate to use coarse-grained continuous space neural field models [1, 7] because these describe the activity measurable by, for example, EEG. An example of a neural field model is the Wilson-Cowan model [33]. The Wilson-Cowan equations describe the neuronal activity of two coupled layers of neurons, one excitatory and one inhibitory [33]. The excitatory neurons increase the activity in the layers while inhibitory neurons decrease the activity of both layers. The combination of excitatory and inhibitory layers is a recipe of complex behaviour that has been observed in numerical simulations and mathematical analysis [7].

The activity in the spatial Wilson-Cowan model decays exponentially in the absence of external input. Both layers are excited by the neurons in the excitatory layer. In contrast to the excitatory layer stands the inhibitory layer inhibiting both layers. Next to the Wilson-Cowan model, we have an adaptive model by Pinto and Ermentrout [21, 22] consisting of an excitatory and an adaptive neural layer. The adaptive layer introduces negative feedback and could represent spike frequency adaptation, synaptic depression, or some other slow process that limits the excitation of the network.

Both models are only excited and inhibited by the neurons more active than a set threshold value. This threshold introduces an activation function into the neural field model describing the relation between the activity of the excitatory and inhibitory neurons and their effect on the rest of the neural field. Rigorous mathematical analysis has been performed on neural field models with a Heaviside activation function [1, 4, 7, 11] because the Heaviside activation function allows for explicit expressions of the existence and stability of standing and travelling bumps and breathers [9, 11]. Analysis has established the existence of bump solutions and moving fronts in one-dimensional neural fields with one excitatory layer [1, 7]. Next to this, the existence of periodic [7, 10, 12] and travelling solutions [11] in one-dimensional neural field models with both excitatory and inhibitory layers have been established. Two-dimensional neural fields have been shown to exhibit breathers and spots [7]. Recent research has shown the existence of these patterns in neural field models with finite transmission speeds [9, 13, 16] and instantaneous delays [9]. Pattern-forming systems in reaction-diffusion systems have been studied intensively [8].

Neuro-biological research suggests that physical neural matter does not behave according to a Heaviside activation function. Realistically, the activation function behaves like a sigmoidal function [18]. Neural field models with a sigmoidal activation function are not tractable to the same mathematical analysis and require numerical tools and have received less attention in comparison to the Heaviside analysis.

Neural field equations with a sigmoidal activation have been treated by Fourier analysis decomposing the synaptic weight function and analysing in Fourier space [2, 29, 30]. Pinto and Ermentrout have used singular perturbation theory to extend the existence of travelling bump solutions to smooth activation functions [21].

Numerical continuation is a tool typically used for the numerical analysis of nonlinear dynamical systems. Numerical continuation has been used to analyse neural field models by Fourier decomposition [10, 24, 26] and Hermite decomposition [26] of the connectivity function. This method is, for example, not applicable for a Gaussian connectivity function because the Gaussian connectivity function does not simplify under Fourier decomposition. For the decomposition to be advantageous, the decomposition of the connectivity function should simplify the problem at hand.

Our interest is the effect of the steepness of the activation function on the existence and stability of patterns in neural fields with a Gaussian connectivity function. Our research question is whether the results of the Heaviside analysis extend to neural fields with a sigmoidal activation function. To investigate this, we develop a numerical continuation scheme to continue standing and travelling bumps and breathers of the neural field with a sigmoidal activation function. Using these numerical tools, we continue steady and periodic solutions of the neural field to find bifurcation diagrams with respect to system parameters.

First, we will introduce the excitatory - inhibitory and adaptive neural field models in sections 2.1, 2.2 and 2.3. Section 2.4 discusses the analysis on the excitatory - inhibitory neural field with a Heaviside activation function. Next, we will describe the numerical continuation tools developed to calculate and continue various patterns of the excitatory - inhibitory model and the adaptive model with a sigmoidal activation function in section 3. This section also concerns the computation of the stability of the calculated patterns. Results of the numerical continuations are presented in section 4. We will reflect on the developed continuation schemes, their performance and the results in section 5. Finally, we will answer our research question by checking the existence and stability of patterns for low values of the slope parameter in section 6.

2 Neural field models

Different neural field models are used to describe spatial neural tissue. This research concerns two different neural field models. The first neural field model consists of two layers of neurons, one excitatory layer and one inhibitory layer. This model will be discussed more in-depth in section 2.1. Next to this model, we will discuss a neural field model with an adaptation layer instead of another neural layer in section 2.2. In section 2.3 we introduce the studied patterns in the neural fields. Finally, section 2.4 consists of the Heaviside analysis of the stationary bump in the excitatory - inhibitory neural field model.

2.1 Excitatory - inhibitory neural field model

The one-dimensional two-layer neural field model consists of an excitatory and an inhibitory layer. The excitatory layer $u_e(x,t)$ excites both layers: high excitation in the excitatory layer results in positive feedback on both the excitatory and the inhibitory layer. The inhibitory layer $u_i(x,t)$ inhibits both layers similar: high excitation in the inhibitory layer results in negative feedback in both layers, Figure 1 shows these relations schematically. The dynamics of the excitatory - inhibitory neural field model are captured in the neural field equations:

$$\begin{cases} \dot{u_e}(x,t) = -u_e(x,t) + \int_{-\infty}^{\infty} w_{ee}(x-y) f_e(u_e(y,t))dy \\ \qquad\qquad - \int_{-\infty}^{\infty} w_{ei}(x-y) f_i(u_i(y,t))dy, \\ \tau \dot{u_i}(x,t) = -u_i(x,t) + \int_{-\infty}^{\infty} w_{ie}(x-y) f_e(u_e(y,t))dy \\ \qquad\qquad - \int_{-\infty}^{\infty} w_{ii}(x-y) f_i(u_i(y,t))dy. \end{cases} \tag{1}$$

Here, the connectivity function is assumed to be Gaussian with strength $\bar{w}_{jk}$ and width σ_{jk}:

$$w_{jk}(z) = \frac{\bar{w}_{jk}}{\sigma_{jk}\sqrt{\pi}} e^{-\left(\frac{z}{\sigma_{jk}}\right)^2}. \tag{2}$$

Furthermore, we assume the activation function f_k to be a sigmoidal function as suggested as introduced by by Wilson & Cowan [32]. The sigmoidal function has steepness parameter $\beta > 0$ and threshold parameter θ_k

$$f_k(u) = \frac{1}{1 + e^{-\beta(u-\theta_k)}}. \tag{3}$$

Examples of the sigmoidal activation function for various values of β are shown in Figure 2.

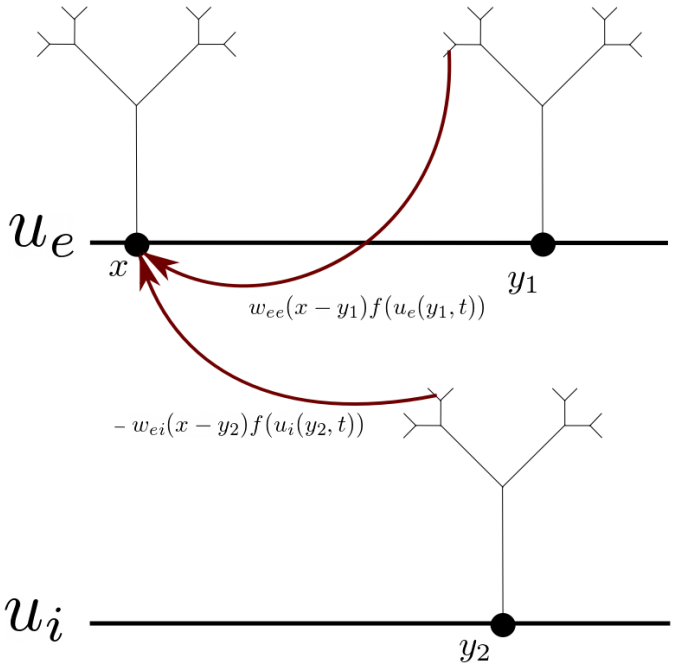

Figure 1: Diagram of a two layer one dimensional neural filed model. Adapted from [7].

2.2 Adaptive neural field

Next to the excitatory - inhibitory neural field model we introduce the adaptive neural field model that has been introduced by Pinto and Ermentrout [21, 22] and consists of an excitatory layer $u(x,t)$ combined with a adaptive layer $a(x,t)$. This adaptive layer introduces negative feedback and could represent spike frequency adaptation, synaptic depression, or some other slow process that limits the excitation of the network. The neural field model is given by

$$\begin{cases} \dot{u}(x,t) = -u(x,t) - \kappa a(x,t) + \int_{-\infty}^{\infty} w(x-y) f(u(y,t)) dy + I(x) \\ \tau \dot{a}(x,t) = -a(x,t) + u(x,t). \end{cases} \tag{4}$$

The synaptic weight function is Gaussian with mean $\bar{w}$ and width σ as introduced in equation (3). The excitation is Gaussian as well and given by

$$I(x) = I_0 e^{-(\frac{x}{\sigma_I})^2}. \tag{5}$$

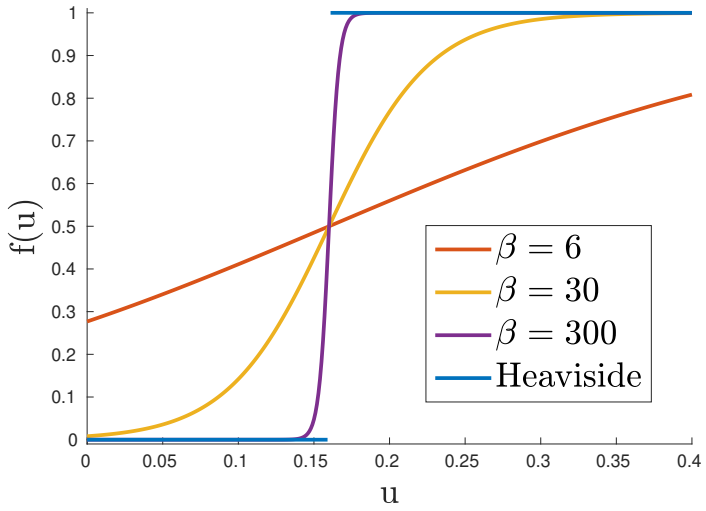

Figure 2: Sigmoidal function with different values of the slope parameter β together with a Heaviside function. The threshold parameter θ_k has been set to 0.16. The domain of the plot depicts typical values of the activity of the neural field.

The adaptive neural field (4) is studied in the β–I_0 parameter space in which standing bump and breather solutions are found [10].

2.3 Patterns in neural field models

Both neural field models (1) and (4) exhibit different patterns in the time evolution [5, 10, 11, 12]. Figure 3 shows simulations of neural field model (1) exhibiting the patterns we will study here. First, the stationary bump solution consisting of a single spatial bump constant in time is plotted in Figure 14a. Next to this, we can find stationary breather solutions which consist of one spatial bump and are periodic in time as illustrated in Figure 14c. Both the stationary bump and breather can drift introducing the travelling bump and the travelling breather in Figure 14b and 14d.

Whilst we study the stationary and travelling bumps and breathers neural field models exhibit more patterns like spatially periodic solutions [14] and sloshing solutions [10].

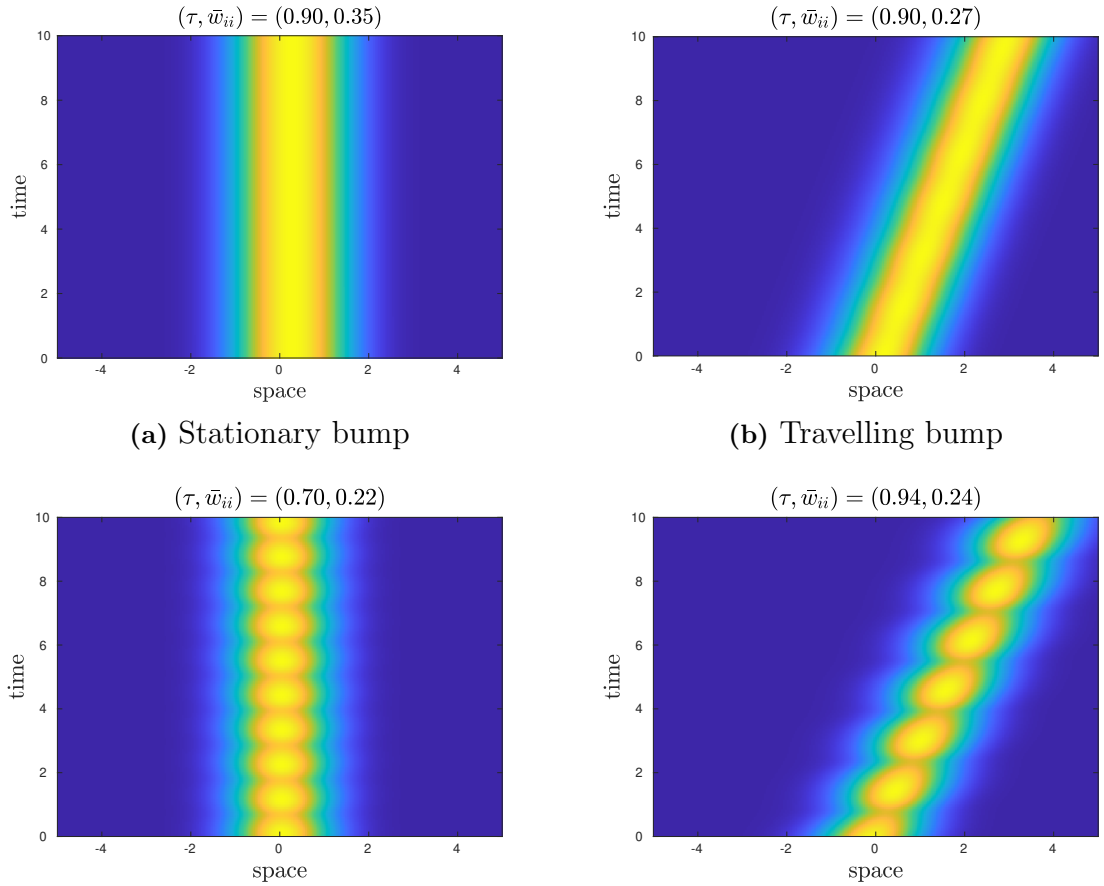

(a) Stationary bump **(b)** Travelling bump

(c) Stationary breather **(d)** Travelling breather

Figure 3: Space-time plots of $u_e(x,t)$ illustrating different solution types. Other parameter values as listed in Table 1

2.4 Heaviside analysis of excitatory - inhibitory neural field

Neural field models with a Heaviside activation function allow for exact analytic expressions for the bump solution. We will show this on the basis of the excitatory - inhibitory neural field model (1) with a Heaviside activation function with threshold values θ_k:

$$f_{h,k}(x) = \begin{cases} 0 & x \leq \theta_k, \\ 1 & x < \theta_k. \end{cases} \tag{6}$$

The Heaviside activation function is shown in Figure 2. We will investigate the existence and the stability of a standing bump solution in section 2.4.1 and section 2.4.2, respectively.

2.4.1 Existence

Stationary bump solutions of neural field (1) require the time derivative to be zero. This results in the implicit solutions

$$\begin{cases} u_e(x) &= \int_{\xi_1^e}^{\xi_2^e} w_{ee}(x-y) f_{h,e}(u_e(y,t))dy - \int_{\xi_1^i}^{\xi_2^i} w_{ei}(x-y) f_{h,i}(u_i(y,t))dy, \\ u_i(x) &= \int_{\xi_1^e}^{\xi_2^e} w_{ie}(x-y) f_{h,e}(u_e(y,t))dy - \int_{\xi_1^i}^{\xi_2^i} w_{ii}(x-y) f_{h,i}(u_i(y,t))dy \end{cases} \tag{7}$$

Here, the threshold values ξ_j^k are the boundaries of the interval where $u_k(x,t) \geq \theta_k$. Because the value of $u_k(x,t)$ is equal to the threshold value θ_k at these boundaries we introduce the existence equations

$$\begin{cases} u_e(\xi_1^e) = \theta_e, \\ u_e(\xi_2^e) = \theta_e, \\ u_i(\xi_1^i) = \theta_i, \\ u_i(\xi_2^i) = \theta_i. \end{cases} \tag{8}$$

By expanding the integrals in equation (7), these solutions can be simplified to

$$\begin{cases} u_e(x) &= \frac{\bar{w}_{ee}}{2}\left[\mathrm{erf}\left(\frac{x-\xi_1^e}{\sigma_{ee}}\right) - \mathrm{erf}\left(\frac{x-\xi_2^e}{\sigma_{ee}}\right)\right] - \frac{\bar{w}_{ei}}{2}\left[\mathrm{erf}\left(\frac{x-\xi_1^i}{\sigma_{ei}}\right) - \mathrm{erf}\left(\frac{x-\xi_2^i}{\sigma_{ei}}\right)\right], \\ u_i(x) &= \frac{\bar{w}_{ie}}{2}\left[\mathrm{erf}\left(\frac{x-\xi_1^e}{\sigma_{ie}}\right) - \mathrm{erf}\left(\frac{x-\xi_2^e}{\sigma_{ie}}\right)\right] - \frac{\bar{w}_{ii}}{2}\left[\mathrm{erf}\left(\frac{x-\xi_1^i}{\sigma_{ii}}\right) - \mathrm{erf}\left(\frac{x-\xi_2^i}{\sigma_{ii}}\right)\right] \end{cases}. \tag{9}$$

We then use the existence equations (8) to verify the self-consistency at the values of ξ_n^k, to find the width of the bump profile.

2.4.2 Stability

The stability of the solution given by equation (9) will be investigated by analysing the propagation of small perturbations of the solution. We assume a perturbation $\tilde{u_k} = u_k + \tilde{\varphi_k}$ and find the first-order propagation of the perturbation by linearising equation (1) around the bump solution (9) to get

$$\begin{cases} \dot{\tilde{\varphi}}_e(x,t) & = -\tilde{\varphi}_e(x,t) + \int_{-\infty}^{\infty} w_{ee}(x-y) f_e'(u_e(y,t))\tilde{\varphi}_e(y,t)dy \\ & \quad - \int_{-\infty}^{\infty} w_{ei}(x-y) f_i'(u_i(y,t))\tilde{\varphi}_i(y,t)dy, \\ \tau\dot{\tilde{\varphi}}_i(x,t) & = -\tilde{\varphi}_e(x,t) + \int_{-\infty}^{\infty} w_{ie}(x-y) f_e'(u_e(y,t))\tilde{\varphi}_e(y,t)dy \\ & \quad - \int_{-\infty}^{\infty} w_{ii}(x-y) f_i'(u_i(y,t))\tilde{\varphi}_i(y,t)dy. \end{cases} \tag{10}$$

Assuming $\tilde{\varphi}_k(x,t) = e^{\lambda t}\varphi_e(x)$ and rearranging terms, we obtain the problem

$$\begin{cases} -\lambda\varphi_e(x) - \varphi_e(x) + \mathcal{N}_{ee}\varphi_e - \mathcal{N}_{ei}\varphi_i & = 0, \\ -\tau\lambda\varphi_e(x) - \varphi_i(x) + \mathcal{N}_{ie}\varphi_e - \mathcal{N}_{ii}\varphi_i & = 0, \end{cases} \tag{11}$$

where $\mathcal{N}_{jk}\varphi_k$ is given by

$$\mathcal{N}_{jk}\varphi_k = \int_{-\infty}^{\infty} w_{jk}(x-y) f_k'(u_k(y,t))\varphi_k(y)dy \tag{12}$$

$$= \int_{-\infty}^{\infty} w_{jk}(x-y)\delta(u_k(y,t) - \theta_k)\varphi_k(y)dy \tag{13}$$

$$= \varphi_k(\xi_1^k)\frac{w_{jk}(x-\xi_1^k)}{\left|u_k'(\xi_1^k)\right|} + \varphi_k(\xi_2^k)\frac{w_{jk}(x-\xi_2^k)}{\left|u_k'(\xi_2^k)\right|}, \tag{14}$$

where we made use of the sifting property of the Dirac delta function.

To identify at which λ equation (11) exhibits non-trivial solutions we try to find solutions to the equation

$$\begin{cases} -(\lambda+1)\varphi_e(x) + \mathcal{N}_{ee}\varphi_e - \mathcal{N}_{ei}\varphi_i & = g_e(x), \\ -(\tau\lambda+1)\varphi_i(x) + \mathcal{N}_{ie}\varphi_e - \mathcal{N}_{ii}\varphi_i & = g_i(x), \end{cases} \tag{15}$$

for some g_k to identify when invertibility fails. Invertibility fails whenever the equations evaluated at the threshold values ξ_n^k with $f_k(\xi_n^k) = \theta_k$ give a singular matrix equation

$$M(\lambda)\boldsymbol{\psi} = \boldsymbol{F}, \tag{16}$$

where

$$M(\lambda) = \begin{bmatrix} -(1+\lambda) + \frac{w_{ee}(0)}{\left|u_e'(\xi_1^e)\right|} & \frac{w_{ee}(\xi_1^e-\xi_2^e)}{\left|u_e'(\xi_2^e)\right|} & -\frac{w_{ei}(\xi_1^e-\xi_1^i)}{\left|u_e'(\xi_1^i)\right|} & -\frac{w_{ei}(\xi_1^e-\xi_2^i)}{\left|u_e'(\xi_2^i)\right|} \\ \frac{w_{ee}(\xi_2^e-\xi_1^e)}{\left|u_e'(\xi_1^e)\right|} & -(1+\lambda) + \frac{w_{ee}(0)}{\left|u_e'(\xi_2^e)\right|} & -\frac{w_{ei}(\xi_2^e-\xi_1^i)}{\left|u_e'(\xi_1^i)\right|} & -\frac{w_{ei}(\xi_2^e-\xi_2^i)}{\left|u_e'(\xi_2^i)\right|} \\ \frac{w_{ie}(\xi_1^i-\xi_1^e)}{\left|u_e'(\xi_1^e)\right|} & \frac{w_{ie}(\xi_1^i-\xi_2^e)}{\left|u_e'(\xi_2^e)\right|} & -(1+\tau\lambda) - \frac{w_{ii}(0)}{\left|u_e'(\xi_1^i)\right|} & -\frac{w_{ii}(\xi_1^i-\xi_2^i)}{\left|u_e'(\xi_2^i)\right|} \\ \frac{w_{ie}(\xi_2^i-\xi_1^e)}{\left|u_e'(\xi_1^e)\right|} & \frac{w_{ie}(\xi_2^i-\xi_2^e)}{\left|u_e'(\xi_2^e)\right|} & -\frac{w_{ii}(\xi_2^i-\xi_1^i)}{\left|u_e'(\xi_1^i)\right|} & -(1+\tau\lambda) - \frac{w_{ii}(0)}{\left|u_e'(\xi_2^i)\right|} \end{bmatrix}, \tag{17}$$

for $\boldsymbol{\psi} = [\varphi_e(\xi_e^1), \varphi_e(\xi_e^2), \varphi_i(\xi_i^1), \varphi_i(\xi_i^2)]^T$ and $\boldsymbol{F} = [g_e(\xi_e^1), g_e(\xi_e^2), g_i(\xi_i^1), g_i(\xi_i^2)]^T$.

When $\det(M(\lambda)) = 0$ holds, equation (15) does not have a solution for all f. In that case there exist non-trivial solutions to equation (11). Therefore, this is an Evans function [7] $\mathcal{E}(\lambda)$ for the standing bump

$$\mathcal{E}(\lambda) = \det[M(\lambda)]. \tag{18}$$

Zeros of $\mathcal{E}(\lambda)$ correspond to eigenvalues of equation (11) and determine the stability of the solution. When we have $\mathrm{Re}(\lambda) < 0$ for all λ satisfying $\mathcal{E}(\lambda) = 0$, we can conclude the bump solution (7) is stable.

Replacing the Heaviside activation function with a sigmoidal activation function leaves us with an equation that does not allow us to perform the same existence and stability analysis because the integrals in equation (1) fail to simplify similarly. To study the existence of stationary and periodic solutions of neural field (1) we will therefore develop a numerical continuation scheme in the next section.

3 Numerical Continuation of patterns in neural fields

Numerical continuation is a well-established method for finding branches of equilibria and limit cycles of dynamical systems with respect to varying parameters [15]. We will develop a numerical continuation scheme to analyse fixed points and limit cycles of the discretised neural field models by numerical continuation based on previous work [15, 17] in section 3.1.

A well-known method for investigating limit cycles is single shooting [15, 17]. However, single shooting methods can have long numerical integration periods in which orbits can end up outside the area in which linear correction tools can be applied. To overcome this problem, we include a discretisation of the full orbit to the continuation variables in section 3.2.3. Including the time evolution of the solution increases the number of variables in our continuation problem by several orders of magnitude. Numerical continuation requires solving a linear system of equations which is efficiently solved by matrix-free methods and we implement matrix-free continuation in section 3.3. The matrix-free method requires us to calculate directional derivatives which can be calculated numerically by finite differences. Section 3.4 investigates the possibilities of calculating these directional derivatives more accurately. To summarise the developed methods, section 3.5 presents an overview of the developed numerical method which will be used in section 3.6 to construct two-parameter bifurcation diagrams. Finally, we will consider the stability of the patterns in section 3.7.

The following sections will make extensive use of time integration of the neural field. This will be denoted by

$$\psi_{t_1}(\boldsymbol{u}) = \int_0^{t_1} F(\boldsymbol{u}, t)dt, \tag{19}$$

which should be read as the time integration of the initial condition $\boldsymbol{u}$ from $t = 0$ up to $t = t_1$. This can, for example, be computed numerically with the fourth-order Runge Kutta scheme [23].

3.1 Numerical continuation

Numerical continuation is a numerical method to find the zeros of a function

$$F(\boldsymbol{x}, \rho) : \mathbb{R}^n \times \mathbb{R} \to \mathbb{R}^n, \tag{20}$$

which, by the Inverse Function Theorem (IFT), lie on a smooth one-dimensional curve. To illustrate the procedure of numerical continuation, we focus on the one-

dimensional dynamical system $\dot{x} = F(x, \rho)$ given by

$$F(x, \rho) = x^3 - x^2 + \rho. \tag{21}$$

The zeros of equation (21) are plotted in Figure 4 and form a smooth manifold by the IFT.

Numerical continuation is an iterative predictor-corrector procedure that extends known zeros of equation (20). First, the continuation direction is determined. Next, a new point on the curve is predicted. Finally, the estimated new point is corrected to obtain a new zero of equation (20). This procedure is then repeated by estimating a new point.

Given two known zeros $(x, \rho)_{i-1}$ and $(x, \rho)_i$ of equation (20), the secant direction $(v_x, v_\rho)_i$ is calculated as

$$(v_x, v_\rho) = (x, \rho)_i - (x, \rho)_{i-1}. \tag{22}$$

This direction is then used to predict a new approximate zero

$$(\tilde{x}, \tilde{\rho})_{i+1} = (\tilde{x}, \rho)_i + h_0 \cdot (v_x, v_\rho) \tag{23}$$

near the curve. The step h_0 size is chosen adaptively such that the number of required correction steps remains small. This process of estimating a new point on the curve is shown in Figure 4(a) and (b).

Finally, Newton corrections are used to correct $(\tilde{x}, \tilde{\rho})_{i+1}$ to a new point $(x, \rho)_{i+1}$ on the curve. Newton's method can be used to solve a system of equations which has an equal number of variables and unknowns. This can either be solved by fixing the parameter ρ and performing Newton iterations on $F(x, \rho)$ for fixed ρ, or by appending an additional scalar equation

$$h(x, \rho) = 0. \tag{24}$$

such that the resulting system

$$G(x, \rho) = \begin{cases} F(x, \rho) = 0, \\ h(x, \rho) = 0, \end{cases} \tag{25}$$

can be solved by Newton iterations. Fixing ρ is called natural continuation and this is discussed further in section 3.1.1. A special choice of $h(x, \rho)$ is known as pseudo-arclength continuation, and this will be discussed in section 3.1.2.

3.1.1 Natural continuation

Natural continuation performs Newton iterations for fixed ρ [17]. These Newton corrections will converge to a zero of equation (20) with the same value of ρ. All points in the x–ρ plane with the same ρ lie on a vertical line shown twice in Figure 4(a).

At regular points, natural continuation converges to the intersection between the dashed line and the $F(x, \rho) = 0$ curve in Figure 4(a). The bottom of Figure 4(a) shows natural continuation at regular zeros. The dashed search line intersects the solution curve and the Newton iterations converge to the intersection.

The top of Figure 4(a) shows natural continuation at a fold bifurcation; because the dashed line does not intersect the sought curve, the Newton iterations will not converge to a point on the curve. Therefore, natural continuation is not suitable to continue curves around a fold bifurcation. This problem is solved by using pseudo-arclength continuation, which will be discussed next.

3.1.2 Pseudo-arclength continuation

Instead of fixing ρ and performing Newton corrections on $F(x, \rho)$, we can append an additional scalar equation (24) such that the resulting system of equations (25) can be solved by Newton iterations. A natural choice [17] of $h(x, \rho)$ is

$$h(x, \rho) = \langle (x, \rho) - (\tilde{x}, \tilde{\rho})_{i+1}, (v_x, v_\rho) \rangle \tag{26}$$

$$= (x - \tilde{x}_{i+1}) v_x + (\rho - \tilde{\rho}_{i+1}) v_\rho, \tag{27}$$

where $\langle \cdot, \cdot \rangle$ denotes the Euclidean inner product. This requires the correction direction to be orthogonal to the prediction direction (v_x, v_ρ), and is called pseudo-arclength continuation [17].

Newton corrections for pseudo-arclength continuation entail the following procedure iteratively, with $(x, \rho)_{i+1,0} = (\tilde{x}, \tilde{\rho})_{i+1}$:

$$b = G((x, \rho)_{i+1,k}) = \begin{bmatrix} F((x, \rho)_{i+1,k} \\ 0 \end{bmatrix} \tag{28}$$

Solve for $[dx, d\rho]^T$:

$$\frac{\partial G((x, \rho)_{i+1,k})}{\partial (x, \rho)} \begin{bmatrix} dx \\ d\rho \end{bmatrix} = b \tag{29}$$

Update x, ρ:

$$(x, \rho)_{i+1,k+1} = (x, \rho)_{i+1,k} - (dx, d\rho) \tag{30}$$

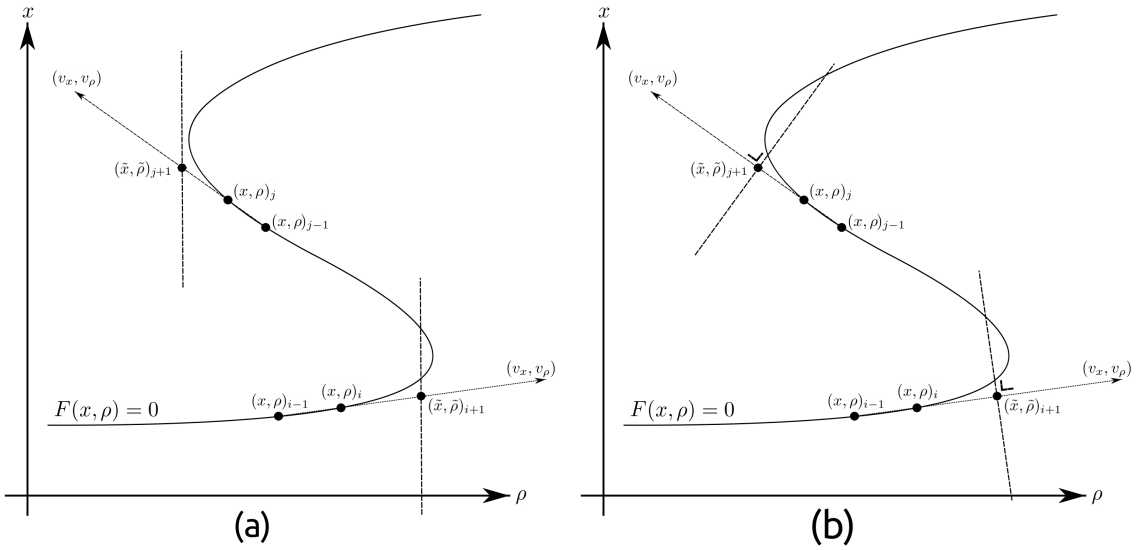

Figure 4: Overview of (a) natural and (b) pseudo-arclength continuation at regular points $(x, \rho)_i$ at the bottom of the figure and folds $(x, \rho)_j$ at the top of the figure. The dashed lines show the subspace in which Newton corrections are performed. The top part of (a) shows that natural continuation fails close to a fold bifurcation because the dashed line does not intersect $F(x, \rho) = 0$, while in the same scenario pseudo-arclength continuation does intersect as shown at the top of (b).

until convergence of $(x, \rho)_{i+1,k}$.

The choice of $h(x, \rho)$ in equation (27) in the context of system (21) makes the directional derivative in equation (29)

$$\frac{\partial G((x,\rho)_{i+1,k})}{\partial(x,\rho)} \begin{bmatrix} dx \\ d\rho \end{bmatrix} = \begin{bmatrix} x_{i+1,k}(3x_{i+1,k} - 2) & 1 \\ v_x & v_\rho \end{bmatrix} \begin{bmatrix} dx \\ d\rho \end{bmatrix} \tag{31}$$

$$= \begin{bmatrix} x_{i+1,k}(3x_{i+1,k} - 2)dx + d\rho \\ v_x dx + v_\rho \rho \end{bmatrix}, \tag{32}$$

where we have made use of F in equation (21). The second row of equation (32) can be interpreted as the requirement that the correction vector $[dx, d\rho]^T$ be orthogonal to the continuation direction $[v_x, v_\rho]^T$, this is denoted by a right angle in Figure 4(b). Figure 4 also shows the difference between natural continuation and pseudo-arclength continuation, at fold bifurcations at the top of both figures. Because the method searches a new point orthogonally, the curve can be continued around the fold bifurcation.

Now that we have introduced numerical continuation with two different correction methods, we will introduce neural field (1) into this framework in the next section.

3.2 Numerical continuation of neural fields

The numerical continuation methods outlined in sections 3.1.1 and 3.1.2 can be extended to higher-dimensional dynamical systems defined by functions

$$F(\boldsymbol{u}, \rho) : \mathbb{R}^n \times \mathbb{R} \to \mathbb{R}^n, \tag{33}$$

by replacing the derivative $\frac{\partial F(x,\rho)}{\partial x}$ in equation (29) with the Jacobian matrix $\frac{\partial F(\boldsymbol{u},\rho)}{\partial \boldsymbol{u}}$.

Using a discretisation of neural field (1)

$$\dot{\boldsymbol{u}} = F(\boldsymbol{u}), \;\; \boldsymbol{u} \in \mathbb{R}^{2\times N_x} \tag{34}$$

with

$$\boldsymbol{u} = \begin{bmatrix} u_e(x_1) \\ u_e(x_2) \\ \vdots \\ u_e(x_{N_x}) \\ u_i(x_1) \\ u_i(x_2) \\ \vdots \\ u_i(x_{N_x}) \end{bmatrix} \tag{35}$$

for some spatial discretisation

$$x_0 \leq x_1 \leq \cdots \leq x_{N_x}, \tag{36}$$

we aim to locate and continue patterns in neural field (1) and (4). Numerical continuation of these patterns is the subject of the following sections.

3.2.1 Numerical continuation of stationary bump solutions

We can identify bump solutions of neural field (1) and (4) as the zeros of

$$F(\boldsymbol{u}) = 0, \tag{37}$$

because this corresponds to zeros of the right hand side of the neural field equations.

However, this does not uniquely describe the stationary bump solutions. Both neural fields (1) and (4) are invariant under translation: given any solution $u(x,t)$ we have a family of solutions $u(x+\alpha,t)$ parametrised by $\alpha \in \mathbb{R}$. In order to disambiguate between the solutions, we impose that the maximum value of $u_e(x,t)$ is attained at $x = 0$. Next to this, we observe that the stationary bump solutions are symmetric around the maximum of the bump, $u(x,t) = u(-x,t)$ for centred bumps. We use this symmetry to implement the disambiguation with respect to translation by employing

a symmetrical spatial discretisation to continue the half space solution

$$\boldsymbol{u}_h = \begin{bmatrix} u_e(x_{N_x/2+1}) \\ u_e(x_{N_x/2+2}) \\ \vdots \\ u_e(x_{N_x}) \\ u_i(x_{N_x/2+1}) \\ u_i(x_{N_x/2+2}) \\ \vdots \\ u_i(x_{N_x}) \end{bmatrix}. \tag{38}$$

To continue the stationary bump of the neural field, we find zeroes of the composition

$$F_h(\boldsymbol{u}_h) = (M^{-1} \circ F \circ M)(\boldsymbol{u}_h). \tag{39}$$

M expands the half solution $\boldsymbol{u}_h$ to a full solution $\boldsymbol{u}$ by mirroring:

$$M(\boldsymbol{u}_h) = \begin{bmatrix} \boldsymbol{u}_{N_x} \\ \vdots \\ \boldsymbol{u}_1 \\ \boldsymbol{u}_1 \\ \vdots \\ \boldsymbol{u}_{N_x} \\ \boldsymbol{u}_{2N_x} \\ \boldsymbol{u}_{2N_x-1} \\ \vdots \\ \boldsymbol{u}_{N_x+1} \\ \boldsymbol{u}_{N_x+1} \\ \vdots \\ \boldsymbol{u}_{2N_x} \end{bmatrix}. \tag{40}$$

Therefore, we can use numerical continuation to locate and continue bump solutions of neural field (1) by continuing the zeroes of equation (39).

3.2.2 Numerical continuation of travelling bump solutions

To continue travelling bump solutions of neural field (1), we introduce co-moving coordinates $\xi = x - ct$ because travelling bump solutions of neural field (1) correspond

with standing bump solutions in co-moving frame. We rewrite the neural field (1) in these travelling wave coordinates to obtain:

$$\begin{cases} \dot{u_e}(\xi,t) = -u_e(\xi,t) + c\frac{\partial u_e}{\partial \xi}(\xi,t) + \int_{-\infty}^{\infty} w_{ee}(\xi-\nu) f_{h,e}(u_e(\nu,t))d\nu \\ \qquad\qquad - \int_{-\infty}^{\infty} w_{ei}(\xi-\nu) f_{h,i}(u_i(\nu,t))d\nu, \\ \tau\dot{u_i}(\xi,t) = -u_i(\xi,t) + c\tau\frac{\partial u_e}{\partial \xi}(\xi,t) + \int_{-\infty}^{\infty} w_{ie}(\xi-\nu) f_{h,e}(u_e(\nu,t))d\nu \\ \qquad\qquad - \int_{-\infty}^{\infty} w_{ii}(\xi-\nu) f_{h,i}(u_i(\nu,t))d\nu. \end{cases} \tag{41}$$

Similar to the stationary bump solution we can locate standing bump solutions by finding zeros of a discretisation $F_{tr\,discr}$ of equation (41) with some spatial discretisation

$$\xi_0 \leq \xi_1 \leq \cdots \leq \xi_{N_x}. \tag{42}$$

However, the travelling bump is not uniquely characterised by the values of $u_k(\xi_i)$. The wave speed should also be considered a continuation parameter. Therefore, we need an additional equation to define the travelling bump uniquely. This equation is provided by the translation symmetry of the neural field. To fix the neural field we fix the maximum of $u_e(x,t)$ at $x = 0$.

Combining this, travelling bump solutions correspond to the zeros of

$$F_{tr}(\boldsymbol{u},\rho) = \begin{bmatrix} F_{tr\,discr}(\boldsymbol{u},\rho) \\ h(\boldsymbol{u}) \end{bmatrix} \tag{43}$$

with

$$\boldsymbol{u} = \begin{bmatrix} u_e(\xi_1) \\ u_e(\xi_2) \\ \vdots \\ u_e(\xi_{N_x}) \\ u_i(\xi_1) \\ u_i(\xi_2) \\ \vdots \\ u_i(\xi_{N_x}) \\ c \end{bmatrix} \tag{44}$$

and

$$h(\boldsymbol{u}) = u_{N_x/2+1} - u_{N_x/2-1} \tag{45}$$

requiring the bump to have a maximum at the origin. The evaluation of the discretised neural field requires the calculation of the derivative $\frac{\partial u_k}{\partial \xi}$ which is calculated

numerically by transforming to Fourier space using FFT, multiplying by $\frac{2\pi\xi}{L}$ and transforming back.

Therefore, we will analyse travelling bump solutions by continuation of the zeros of

$$F_{tr}(\boldsymbol{u}, \rho) = 0. \tag{46}$$

Periodic solutions can be located and continued similar to stationary solutions. We will elaborate on this in the next section.

3.2.3 Numerical continuation of stationary periodic orbits

Continuation of periodic orbits is best understood in a single shooting context where we require

$$\psi_{T_0}(\boldsymbol{u}) - \boldsymbol{u} = 0, \tag{47}$$

together with a phase condition $g(\boldsymbol{u}) = 0$ to remove the time invariance. This method is prone to convergence issues for unstable orbits because the numerical integration can evolve outside the area where linear corrections suffice. To improve numerical stability for these orbits we choose $N_t, n \in \mathbb{N}$ and set $\Delta t = \frac{T_0}{nN_t}$ to introduce a time mesh

$$t_i = in\Delta t \qquad i \in [1, \cdots, N_t] \tag{48}$$

such that $t_0 = 0$ and $t_{N_t} = T_0$. We include the sections $\boldsymbol{u}_{t_i} = \psi_{t_i}(\boldsymbol{u})$ to the continuation variables. By adding enough intermediate sections, the integration is only affected by the local divergence. This is because we only require numerical integration over a short period of T_0/N_t in which the numerical integration does not diverge too much. The situation has been plotted schematically in Figure 5.

Combining the variables $\boldsymbol{u}_i$ and T_0 into one vector with all variables gives us

$$\boldsymbol{u} = \begin{bmatrix} \boldsymbol{u}_{t_0} \\ \boldsymbol{u}_{t_1} \\ \vdots \\ \boldsymbol{u}_{t_{N_t-1}} \\ \boldsymbol{u}_{t_{N_t}} \\ T_0 \end{bmatrix}. \tag{49}$$

Similar to the continuation of stationary bump solutions, we break the spatial translational invariance by introducing the half space discretisation used for the continuation

of stationary bump solutions. Therefore, the continued half space variables are

$$\boldsymbol{u}_h = \begin{bmatrix} \boldsymbol{u}_{h,t_0} \\ \boldsymbol{u}_{h,t_1} \\ \vdots \\ \boldsymbol{u}_{h,t_{N_t-1}} \\ \boldsymbol{u}_{h,t_{N_t}} \\ T_0 \end{bmatrix}. \tag{50}$$

The numerical integration is performed in full space variables by composition with the mirroring function M and its inverse defined in equation (40)

$$\psi^h_{h,n\Delta t}(\boldsymbol{u}_{t_0}) = (M^{-1} \circ \psi_{n\Delta t} \circ M)(\boldsymbol{u}_{h,t_i}). \tag{51}$$

Finally, to uniquely define the periodic orbits, a periodicity condition $\boldsymbol{u}_{N_t n\Delta t} - \boldsymbol{u}_0 = 0$, and a phase condition $g(\boldsymbol{u}) = 0$ are required. Periodic solutions with period T_0 of equation (34) are then the zeros of

$$F^{hist}_{per}(\boldsymbol{u}_h, \rho) = F^{hist}_{per}(\begin{bmatrix} \boldsymbol{u}_{h,t_0} \\ \boldsymbol{u}_{h,t_1} \\ \vdots \\ \boldsymbol{u}_{h,t_{N_t-1}} \\ \boldsymbol{u}_{h,t_{N_t}} \\ T_0 \end{bmatrix}) = \begin{bmatrix} \psi^h_{n\Delta t}(\boldsymbol{u}_{h,t_0}) - \boldsymbol{u}_{h,t_1} \\ \psi^h_{n\Delta t}(\boldsymbol{u}_{h,t_1}) - \boldsymbol{u}_{h,t_2} \\ \vdots \\ \psi^h_{n\Delta t}(\boldsymbol{u}_{h,t_{N_t-1}}) - \boldsymbol{u}_{h,t_{N_t}} \\ \boldsymbol{u}_{t_{h,N_t}} - \boldsymbol{u}_{h,t_0} \\ g(\boldsymbol{u}_h) \end{bmatrix} \tag{52}$$

with the phase condition $g(\boldsymbol{u})$ given by

$$g(\boldsymbol{u}_h) = \langle \boldsymbol{u}_{h,t_0} - \boldsymbol{u}^r_{h,t_0}, \dot{\boldsymbol{u}}^r_{h,t_0} \rangle \tag{53}$$

with respect to a reference solution $\boldsymbol{u}^r_{h,t_0}$ to ensure uniqueness along the periodic solution. This reference solution is taken to be the previous solution along the solution branch.

3.2.4 Numerical continuation of travelling periodic orbits

Similarly to the continuation of stationary periodic orbits, we can identify travelling periodic orbits by applying a single shooting method to the neural field in travelling wave coordinates (41).

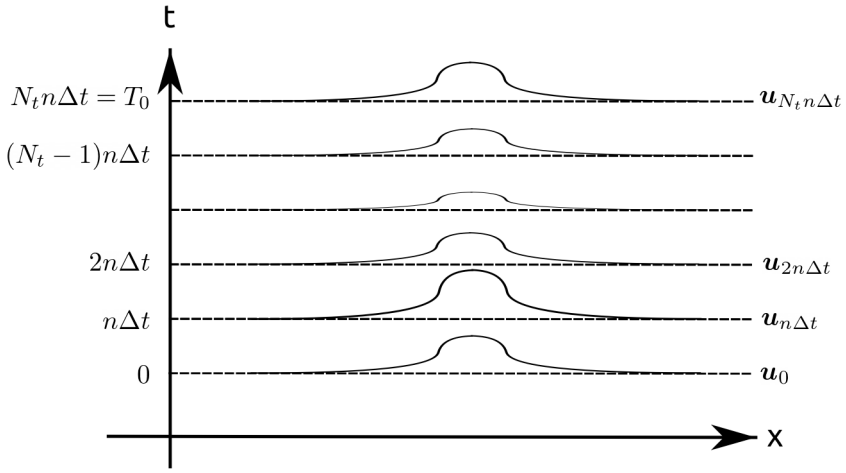

Figure 5: Schematic overview of the variables in Equation (54).

Analogous to the continuation of travelling bumps outlined in section 3.2.2 the wave speed is added to the system variables and we arrive at

$$\boldsymbol{u} = \begin{bmatrix} \boldsymbol{u}_{t_0} \\ T_0 \\ c \end{bmatrix}. \tag{54}$$

The travelling breather solutions correspond to the zeros of

$$F^{tr}_{per}(\boldsymbol{u}) = F^{tr}_{per}\left(\begin{bmatrix} \boldsymbol{u}_{t_0} \\ T_0 \\ c \end{bmatrix}\right) = \begin{bmatrix} \psi_{T_0}(\boldsymbol{u}_{t_0}) - \boldsymbol{u}_{t_0} \\ g(\boldsymbol{u}) \\ h(\boldsymbol{u}) \end{bmatrix} \tag{55}$$

with phase condition (53) and shift condition (45).

3.3 Matrix free continuation

Introducing the time evolution at a time mesh results in a numerical continuation problem much larger than the original problem due to the discretisation: $\boldsymbol{u}$ in equation (52) has dimension $2 \times N_x \times (N_t + 1) + 1$ which can be very high. Continuation outlined in section 3.1 requires iterative calculation of the Jacobian matrix A to solve $A\boldsymbol{u} = b$ until convergence [15].

For these large problems, explicit calculation of the Jacobian matrix is no longer feasible. To approximate the solution to $A\boldsymbol{u} = b$, matrix-free methods based on Krylov

subspace methods can be employed [28, 31]. These iterative methods employ matrix-vector products $A\boldsymbol{u}$, which are, in the context of continuation, directional derivatives in the direction of $\boldsymbol{u}$ at $\boldsymbol{u}_0$. These directional derivatives can be approximated by $A\boldsymbol{u} = \frac{F(\boldsymbol{u}_0+h\boldsymbol{u})-F(\boldsymbol{u}_0-h\boldsymbol{u})}{2h}$ for some $h > 0$ or by a more sophisticated method, which will be outlined in section 3.4.

We will employ GMRES since it is the most widely used linear solver for non-symmetric problems [28]. To increase the convergence of GMRES we use a simple preconditioner which re-scales β to β_0 where $\beta = \beta_0\beta^*$ with $\beta^* = 500$. This ensures that all elements of $\boldsymbol{u}$ are between 0 and 1.

However, the convection term in travelling wave coordinates (41) results in a line spectrum in the complex plane [11]. This unbounded spectrum greatly impacts the convergence of GMRES [28]. Therefore, GMRES will only be employed for stationary bumps and breathers.

3.4 Exact directional derivative

The matrix-free continuation requires the iterative calculation of the directional derivative and can be approximated numerically using finite differences. However, we may attempt to calculate the directional derivative more accurately for the continuation of fixed points and periodic orbits. To archive this, we will first derive the Jacobian matrix of the discrete neural field (34) in section 3.4.1. Next, we will look at the derivative of $\psi_t(\boldsymbol{u})$ with respect to $\boldsymbol{u}$ in section 3.4.2. We will combine these results in section 3.4.3. Finally, section 3.4.4 will put this into the context of continuation.

3.4.1 Directional derivative of the neural field

The directional derivative of equation (34) can be obtained exactly by employing the convolution in neural field (1) to obtain

$$\begin{aligned} J_{\boldsymbol{u}}\boldsymbol{v} &= \frac{\partial}{\partial[\boldsymbol{u}_e, \boldsymbol{u}_i]} \begin{bmatrix} -\boldsymbol{u}_e + w_{ee} \circledast f_e(\boldsymbol{u}_e) - w_{ei} \circledast f_i(\boldsymbol{u}_i) \\ -\boldsymbol{u}_i/\tau + w_{ie} \circledast f_e(\boldsymbol{u}_e)/\tau - w_{ii} \circledast f_i(\boldsymbol{u}_i)/\tau \end{bmatrix} \begin{bmatrix} \boldsymbol{v}_e \\ \boldsymbol{v}_i \end{bmatrix} \\ &= \begin{bmatrix} -1 + w_{ee} \circledast f_e'(\boldsymbol{u}_e) & -w_{ei} \circledast f_i'(\boldsymbol{u}_i) \\ w_{ie} \circledast f_e'(\boldsymbol{u}_e)/\tau & -1/\tau - w_{ii} \circledast f_i'(\boldsymbol{u}_i)/\tau \end{bmatrix} \begin{bmatrix} \boldsymbol{v}_e \\ \boldsymbol{v}_i \end{bmatrix} \\ &= \begin{bmatrix} -\boldsymbol{v}_e + w_{ee} \circledast f_e'(\boldsymbol{u}_e)\boldsymbol{v}_e - w_{ei} \circledast f_i'(\boldsymbol{u}_i)\boldsymbol{v}_i \\ -\boldsymbol{v}_i/\tau + w_{ie} \circledast f_e'(\boldsymbol{u}_e)\boldsymbol{v}_e/\tau - w_{ii} \circledast f_i'(\boldsymbol{u}_i)\boldsymbol{v}_i/\tau \end{bmatrix} \end{aligned} \tag{56}$$

where $\circledast$ denotes spatial convolution. Similarly, the directional derivative of the adaptive neural field in the direction $\boldsymbol{v} = \begin{bmatrix} \boldsymbol{v}_u \\ \boldsymbol{v}_a \end{bmatrix}$ can be expressed as

$$J_{\boldsymbol{u}}\boldsymbol{v} = \begin{bmatrix} -\boldsymbol{v}_u - \kappa \boldsymbol{v}_a + \bar{w}_e \circledast f'(\boldsymbol{u})\boldsymbol{v}_u \\ -\boldsymbol{v}_a/\tau + \boldsymbol{v}_u/\tau \end{bmatrix}. \tag{57}$$

This directional derivative can be evaluated exactly and can be used for numerical continuation of stationary bump solutions. Next to this, the exact directional derivative is used to find the directional derivative of the time evolution with respect to initial conditions which is the subject of the next section.

3.4.2 Directional derivative of the time evolution

Let us focus on the Jacobian matrix

$$\frac{\partial \psi_T(\boldsymbol{u})}{\partial \boldsymbol{u}}, \tag{58}$$

the derivative of the time evolution from 0 to T with respect to the initial conditions $\boldsymbol{u}$. The end time T is generally independent of the period T_0. To calculate this Jacobian matrix, we need the solution itself which is

$$\boldsymbol{u}(t) = \psi_t(\boldsymbol{u}) \tag{59}$$

and is assumed to be known. To find an exact expression of equation (58), we introduce the variational matrix $Y^{\boldsymbol{u}}$ given by the initial value problem

$$\begin{cases} \dot{Y}^{\boldsymbol{u}}(t) &= J_{\boldsymbol{u}(t)} Y^{\boldsymbol{u}}(t), \\ Y^{\boldsymbol{u}}(0) &= I_n, \end{cases} \tag{60}$$

where $J_{\boldsymbol{u}(t)}$ the Jacobian matrix is of equation (34) at position $\boldsymbol{u}(t)$. $Y^{\boldsymbol{u}}(t)\boldsymbol{v}$ describes the propagation of an initial perturbation $\boldsymbol{v}$ during the integration along the periodic orbit up to time t. Therefore, the directional derivative of $\psi_T(\boldsymbol{u})$ in the direction $\boldsymbol{v}$ is given by

$$\boldsymbol{v}(T) = Y^{\boldsymbol{u}}(T)\boldsymbol{v}. \tag{61}$$

To compute the value of $Y^{\boldsymbol{u}}(T)\boldsymbol{v}$, we reduce the initial value problem (60) to

$$\begin{cases} \dot{\boldsymbol{v}}(t) &= J_{\boldsymbol{u}(t)} \boldsymbol{v}(t), \\ \boldsymbol{v}(0) &= \boldsymbol{v}. \end{cases} \tag{62}$$

To evaluate the directional derivative $J_{\boldsymbol{u}(t))}\boldsymbol{v}(t)$, we employ the exact directional derivative from equation (57). This gives us an exact variational equation for the directional derivative of $\psi_T(\boldsymbol{u})$

$$\boldsymbol{v}(T) = \frac{\partial \psi_T(\boldsymbol{u})}{\partial \boldsymbol{u}}\boldsymbol{v}, \tag{63}$$

where $\boldsymbol{v}(T)$ solves the initial value problem (62). The required numerical integration is performed with the fourth-order Runge Kutta method.

3.4.3 Directional derivative of multiple shooting

To calculate the directional derivative of equation (52) in direction $\boldsymbol{v}$, we expand its full Jacobian matrix with respect to the coordinate vector (54):

$$\begin{aligned} J_{per}^{hist} &= \begin{bmatrix} \frac{\partial[\psi_{\Delta t}(\boldsymbol{u}_0)-\boldsymbol{u}_{n\Delta t}]}{\partial \boldsymbol{u}0} & \frac{\partial[\psi_{\Delta t}(\boldsymbol{u}_0)-\boldsymbol{u}_{n\Delta t}]}{\partial \boldsymbol{u}1} & \frac{\partial[\psi_{\Delta t}(\boldsymbol{u}_0)-\boldsymbol{u}_{n\Delta t}]}{\partial \boldsymbol{u}2} & \cdots & \frac{\partial[\psi_{\Delta t}(\boldsymbol{u}_0)-\boldsymbol{u}_{n\Delta t}]}{\partial T_0} \\ \frac{\partial[\psi_{\Delta t}(\boldsymbol{u}_{n\Delta t})-\boldsymbol{u}_{2n\Delta t}]}{\partial \boldsymbol{u}0} & \frac{\partial[\psi_{\Delta t}(\boldsymbol{u}_{n\Delta t})-\boldsymbol{u}_{2n\Delta t}]}{\partial \boldsymbol{u}1} & \frac{\partial[\psi_{\Delta t}(\boldsymbol{u}_{n\Delta t})-\boldsymbol{u}_{2n\Delta t}]}{\partial \boldsymbol{u}2} & \cdots & \frac{\partial[\psi_{\Delta t}(\boldsymbol{u}_{n\Delta t})-\boldsymbol{u}_{2n\Delta t}]}{\partial T_0} \\ & & \vdots & & \\ \frac{\partial[\psi_{\Delta t}(\boldsymbol{u}_{N_t-1})-\boldsymbol{u}_{N_t n\Delta t}]}{\partial \boldsymbol{u}_0} & \frac{\partial[\psi_{\Delta t}(\boldsymbol{u}_{N_t-1})-\boldsymbol{u}_{N_t n\Delta t}]}{\partial \boldsymbol{u}_{n\Delta t}} & \frac{\partial[\psi_{\Delta t}(\boldsymbol{u}_{N_t-1})-\boldsymbol{u}_{N_t n\Delta t}]}{\partial \boldsymbol{u}_{2n\Delta t}} & \cdots & \frac{\partial[\psi_{\Delta t}(\boldsymbol{u}_{N_t-1})-\boldsymbol{u}_{N_t n\Delta t}]}{\partial T_0} \\ \frac{\partial[\boldsymbol{u}_{N_t n\Delta t}-\boldsymbol{u}_0]}{\partial \boldsymbol{u}0} & \frac{\partial[\boldsymbol{u}_{N_t n\Delta t}-\boldsymbol{u}_0]}{\partial \boldsymbol{u}1} & \frac{\partial[\boldsymbol{u}_{N_t n\Delta t}-\boldsymbol{u}_0]}{\partial \boldsymbol{u}2} & \cdots & \frac{\partial[\boldsymbol{u}_{N_t n\Delta t}-\boldsymbol{u}_0]}{\partial T_0} \\ \frac{\partial g(\boldsymbol{u})}{\partial \boldsymbol{u}0} & \frac{\partial g(\boldsymbol{u})}{\partial \boldsymbol{u}1} & \frac{\partial g(\boldsymbol{u})}{\partial \boldsymbol{u}2} & \cdots & \frac{\partial g(\boldsymbol{u})}{\partial T_0} \end{bmatrix} \\ &= \begin{bmatrix} Y^{x_0}(\Delta t) & -Id & 0 & \cdots & 0 & F(\boldsymbol{u}_{n\Delta t})/N_t \\ 0 & Y^{x_1}(\Delta t) & -Id & \cdots & 0 & F(\boldsymbol{u}_{2n\Delta t})/N_t \\ & & \vdots & & & \\ 0 & 0 & 0 & \cdots & -Id & F(\boldsymbol{u}_{N_t n\Delta t})/N_t \\ -Id & 0 & 0 & \cdots & Id & 0 \\ \dot{\boldsymbol{u}}_r & 0 & 0 & \cdots & 0 & 0 \end{bmatrix}. \end{aligned} \tag{64}$$

Here we have employed the phase condition $g(\boldsymbol{u})$ from equation (53); the Jacobian matrix of $\psi_{n\Delta t}(\boldsymbol{u}_{mn\Delta t})$ from equation (61); and the value of $\frac{\partial \psi_{\Delta t}(\boldsymbol{u}_i)}{\partial T_0}$ is given by applying the fundamental theorem of calculus to equation (19).

Finally, we combine the obtained results to arrive at the exact directional derivative $J_{per}^{hist}\boldsymbol{v}$

$$J_{per}^{hist}\boldsymbol{v} = \begin{bmatrix} Y^{x_0}(\Delta t) & -Id & 0 & \cdots & 0 & F(\boldsymbol{u}_{n\Delta t})/N_t \\ 0 & Y^{x_1}(\Delta t) & -Id & \cdots & 0 & F(\boldsymbol{u}_{2n\Delta t}/N_t) \\ & & \vdots & & & \\ 0 & 0 & 0 & \cdots & -Id & F(\boldsymbol{u}_{N_t n\Delta t})/N_t \\ -Id & 0 & 0 & \cdots & Id & 0 \\ \dot{\boldsymbol{u}}_r & 0 & 0 & \cdots & 0 & 0 \end{bmatrix} \begin{bmatrix} \boldsymbol{v}_0 \\ \boldsymbol{v}_1 \\ \boldsymbol{v}_2 \\ \vdots \\ v_{T_0} \end{bmatrix} \tag{65}$$

$$= \begin{bmatrix} Y^{x_0}(\Delta t)\boldsymbol{v}_0 - \boldsymbol{v}_1 + F(\boldsymbol{u}_{n\Delta t})\frac{v_{T_0}}{N_t} \\ Y^{x_1}(\Delta t)\boldsymbol{v}_1 - \boldsymbol{v}_2 + F(\boldsymbol{u}_{2n\Delta t})\frac{v_{T_0}}{N_t} \\ \vdots \\ Y^{x_{N_t-1}}(\Delta t)\boldsymbol{v}_{N_t-1} - \boldsymbol{v}_{N_t} + F(\boldsymbol{u}_{N_t n\Delta t})\frac{v_{T_0}}{N_t} \\ \boldsymbol{v}_{N_t} - \boldsymbol{v}_0 \\ \langle \dot{\boldsymbol{u}}_r, \boldsymbol{v}_0 \rangle \end{bmatrix}. \tag{66}$$

Therefore, we have an exact expression of $\frac{\partial F_{per}^{hist}(\boldsymbol{u},\rho)}{\partial \boldsymbol{u}}\boldsymbol{v}$. The usage of exact directional derivatives in matrix free continuation is the subject of the next section.

3.4.4 Using exact directional derivatives for matrix-free continuation

Continuation of the discretised neural field requires us to choose between natural continuation and pseudo-arclength continuation. To be able to perform natural continuation we solely the directional derivative $\frac{\partial F(\boldsymbol{u},\rho)}{\partial \boldsymbol{u}}d\boldsymbol{u}$ which can be calculated by using exact directional derivatives.

On the other hand, we have pseudo-arclength continuation. For this, we would need exact values of the directional derivatives derivatives $\frac{\partial F(\boldsymbol{u},\rho)}{\partial \boldsymbol{u}}d\boldsymbol{u}$ and $\frac{\partial F(\boldsymbol{u},\rho)}{\partial \rho}d\rho$ in equation (29), An exact expression of $\frac{\partial F(\boldsymbol{u},\rho)}{\partial \boldsymbol{u}}$ has been obtained in equation (66), to get an exact expression of $\frac{\partial F(\boldsymbol{u},\rho)}{\partial \rho}d\rho$ we would need to evaluate the effect of changing parameters on $\psi_t(\boldsymbol{u})$, which is not trivial. Therefore, we cannot use an exact expression of the directional derivative for pseudo-arclength continuation.

To calculate the complete solution branches for the different patterns, we use a combination of natural continuation and pseudo-arclength continuation. We use natural continuation by default. However, we cannot continue the pattern through a fold bifurcation or close to a Hopf bifurcation of a steady state. To overcome this, we switch temporarily to pseudo-arclength using finite differences whenever the Newton

corrections of natural continuation fail to converge. By adaptively changing the continuation method we, can make use of the best of two worlds: on the one hand, we make use of the speed improvements of exact directional derivatives and on the other hand, we can continue across fold bifurcations whenever required.

3.5 Overview of continuation schemes

To continue patterns in neural field (1) we use a different defining system per pattern. Stationary bumps are continued using $F_h(\boldsymbol{u}, \rho)$ defined in equation (39). Travelling bump solutions are continued in travelling wave coordinates using $F_{tr}(\boldsymbol{u}, \rho)$ in equation (46). Stationary breathers are continued in a multiple shooting setting with $F_{per}^{hist}(\boldsymbol{u}, \rho)$ defined in equation (52). Finally, travelling breathers are continued in a single shooting setting $F_{per}^{tr}(\boldsymbol{u})$ in equation (55). A single shooting setting is used to ensure convergence using GMRES.

To obtain the continuation direction, we use a numerically inexpensive secant approximation [15]. The two points required for the initialisation are obtained by fixing the continuation parameter ρ and perturbing it to obtain a different parameter value $\rho' = \rho + h_\rho$. Newton corrections are performed with fixed ρ and ρ' to obtain the corresponding zeros $\boldsymbol{u}$ and $\boldsymbol{u}'$. These two zeros can then be used to find the first continuation direction $\boldsymbol{v} = (\boldsymbol{u} - \boldsymbol{u}')/||\boldsymbol{u} - \boldsymbol{u}'||$ and start the continuation process.

Continuation is generally performed by natural continuation. Whenever this fails to converge, we switch to pseudo-arclength continuation. After three successful continuation steps, we switch back to natural continuation. The corrections of the stationary bumps and stationary breathers are calculated by GMRES with a suitable rescaling of β if this parameter is part of the continuation problem. Travelling bumps and travelling breathers are corrected using full Jacobian corrections.

The step size h is chosen adaptively such that if the number of corrector steps is larger than the preferred number of corrector steps, the step size is decreased for the next iteration and the step size increases if the number of correction steps is small. Whenever the correction step of the continuation fails we half the step size such that the estimated new point is closer to the sought curve. The step size is bounded to be within a predetermined interval $[h_{min}, h_{max}]$. Whenever the step size increases above h_{max} the step size is set equal to h_{max}. In case the step size decreases below h_{min} the continuation is halted.

3.6 Two parameter bifurcation diagrams

We aim to obtain the two-parameter bifurcation diagrams in both the τ–$\bar{w}_{ii}$ parameter plane to compare to Folias [11] and β–$\bar{w}_{ii}$ parameter spaces of neural field (1) and in the β–I_0 parameter plane of neural field (4) to quantify the effect of the slope parameter. Numerical continuation of codimension one bifurcations would require the calculation of second-order derivatives [17, 20]. These calculations are numerically very expensive and have therefore not been implemented. To obtain these bifurcation diagrams, we scan the parameter space making use of the developed continuation schemes to mark the bifurcations in the two-parameter bifurcation diagrams.

Different scanning procedures are used to map parameter space. The different scanning procedures are shown in Figure 6 and consist of scanning between two parallel bifurcation curves, along a diagonal bifurcation curve, and a procedure to scan along a horizontal or vertical bifurcation curve. This way, by using meshes, we can find a complete bifurcation diagram. Codimension two bifurcations cannot be located directly but we can use our scanning procedures to locate it up to the chosen mesh size.

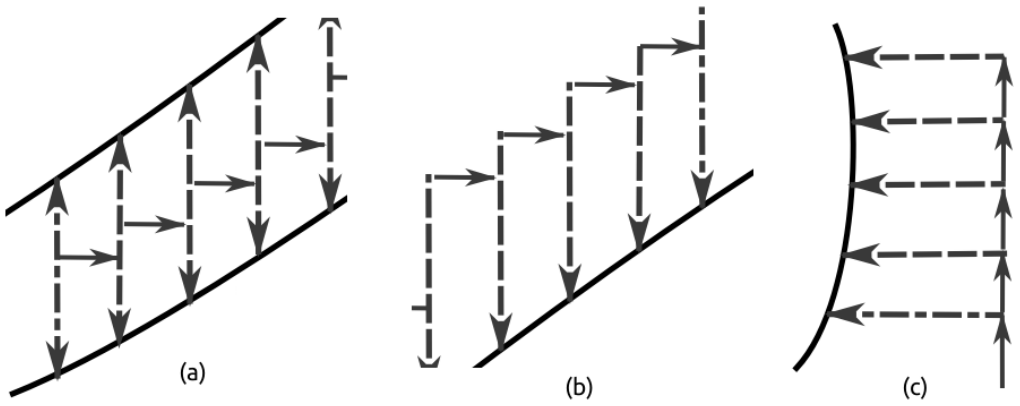

Figure 6: Schematic overview of the scanning approaches used for between two bifurcation curves in parameter space. (a) shows a scanning procedure to scan between two bifurcation curves. (b) shows the scanning procedure for scanning along diagonal bifurcation curves. Finally, (c) shows the scanning along (mostly) horizontal or vertical bifurcation curves.

3.7 Stability analysis of numerical solutions

During the stability analysis of the Heaviside problem in section 2.4.2, we encountered the integral equation (12). This integral could be calculated explicitly by simplifying the integral over the Dirac delta function. However, we cannot use this approach for a Gaussian activation function (3). Therefore, we will calculate the stability of the patterns by analysing the spectrum of the Jacobian.

Applying neural field (1) defines a finite-dimensional system of equations for the numerical solution

$$\dot{\boldsymbol{u}} = F(\boldsymbol{u}(\boldsymbol{x})) \tag{67}$$

for some function F. The stability of this finite dimensional dynamical system can be calculated by analysing the Jacobian $A(\boldsymbol{x}) = \frac{\partial F}{\partial \boldsymbol{x}}$. The solution $\boldsymbol{u}$ is stable if all eigenvalues $\lambda_1, \lambda_2, \lambda_3, \ldots \lambda_n$, of A satisfy $\mathrm{Re}[\lambda] < 0$ [15].

The stability of periodic orbits can be derived from the eigenvalues of the Monodromy matrix $M^{\boldsymbol{u}}(T_0)$ given by the initial value problem

$$\begin{cases} \dot{M}^{\boldsymbol{u}}(t) & = J_{\boldsymbol{u}(t)} Y^{\boldsymbol{u}}(t), \\ M^{\boldsymbol{u}}(0) & = I_n, \end{cases} \tag{68}$$

defined similarly to the variational formulation for directional derivatives explored in section 3.4.2. The eigenvalues of the Monodromy matrix describe the stability of the continued cycle. The periodic orbit is stable if all eigenvalues of the Monodromy matrix lie in the unit circle [3].

4 Results

The numerical continuation schemes outlined in section 3 have been implemented in MATLAB. We start with numerical simulations of neural field (1) and an investigation into the optimal spatial discretisation in section 4.1.1. After this, the single parameter scanning results are extended to the complete τ–$\bar{w}_{ii}$ and β–$\bar{w}_{ii}$ parameter spaces in section 4.1.2. Finally, section 4.2 contains the simulations, single parameter continuations and scanning results of the neural field with adaptation (4).

4.1 Excitatory - inhibitory Neural field

The excitatory - inhibitory neural field (1) has been simulated and continued making use of the MATLAB implementation of the methods described in section 3.

Parameter	Default value
$\bar{w}_{ee}$	1
$\bar{w}_{ei}$	0.84
$\bar{w}_{ie}$	0.8
$\bar{w}_{ii}$	0.265
σ_{ee}	1
σ_{ei}	1
σ_{ie}	1.3
σ_{ii}	1
θ_e	0.16
θ_i	0.24
τ	0.84
β	500

Setting	Default value
N_x	512
Correction threshold	10^{-6}
GMRES maximum iterations	500
GMRES convergence threshold	10^{-10}
Time steps per section n	4
N_t	20
Continuation steps with pseudo-arclength continuation after failed natural continuation	3
Maximum step size h_{max}	0.05
Minimum step size h_{min}	10^{-6}

Table 1: Default values of parameters and continuation settings.

4.1.1 Spatial discretisation

Different patterns have been integrated numerically at different parameter values, these are plotted in Figure 3. Travelling breather solutions vary throughout the τ – $\bar{w}_{ii}$ plane, to illustrate this two different travelling breathers are shown in Figure 7(a) and 7(b). We have taken $c > 0$, which implies right travelling waves for the travelling wave coordinates introduced in section 3.2.2.

Several different patterns have been continued varying a single parameter to investigate numerical convergence with respect to the spatial mesh. Stationary bumps

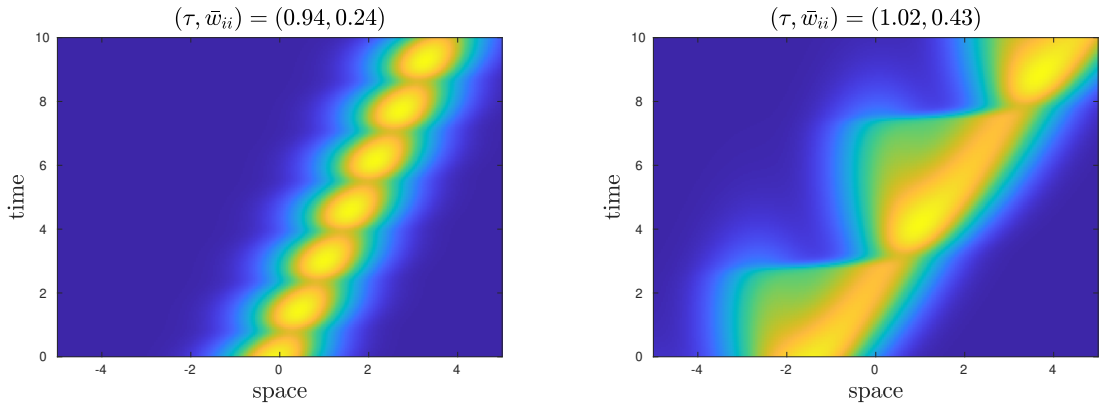

(a) Travelling breather **(b)** Travelling breather for high $\bar{w}_{ii}$

Figure 7: Space-time plots of $u_e(x,t)$ illustrating different travelling breathers. Other parameter values as listed in Table 1

have been continued with respect to $\bar{w}_i i$. The maximum value of the bump along the continued curve has been plotted for $N_x \in \{128, 256, 512, 1024\}$ in figure 8. Spatial discretisations with $N_x \geq 256$ all have very similar results, therefore we can use a spatial discretisation of $N_x = 256$.

The stationary breather has been continued with respect to $\bar{w}_{ii}$ in Figure 9 to determine the optimal spatial discretisation, the maximum and minimum values of the peak along the breather are shown. For $N_x \geq 512$ the results are qualitatively similar and we will use spatial discretisations with $N_x \geq 512$.

Breathers in neural field (1) have been continued with respect to τ at different spatial discretisations. Figure 9 shows continuations started at parameter values listed in table 1.

4.1.2 Two parameter bifurcation diagrams

The τ–$\bar{w}_{ii}$ parameter space has been scanned using the scanning procedures discussed in section 3.6. For $\beta = 500$, the scanned bifurcation diagram is shown in Figure 10a. The bifurcation diagram shows a drift-Hopf bifurcation suggested by Folias[11]. An drift curve of breathers emerges from this drift-Hopf curve which crosses the Fold of stationary breathers. The curve has been calculated up to $\bar{w}_{ii} = 0.33$ due to instability in the continuation of travelling breathers. We also observe the stationary breathers emerging from the red Hopf curve of stationary bumps destabilizes through a dark

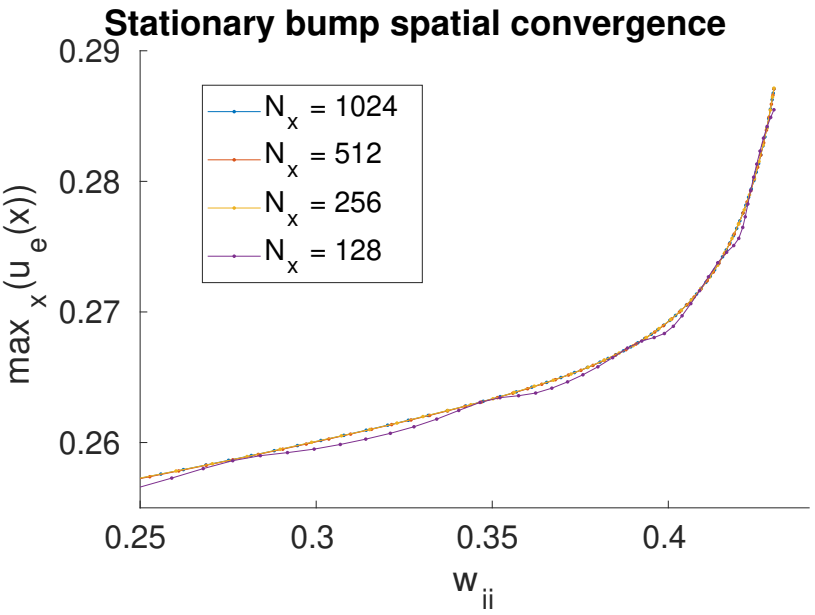

Figure 8: Convergence of numerical scheme for different values of N_x for the stationary bump. The curves have been continued with respect to $\bar{w}_{ii}$, other parameters are as listed in Table 1.

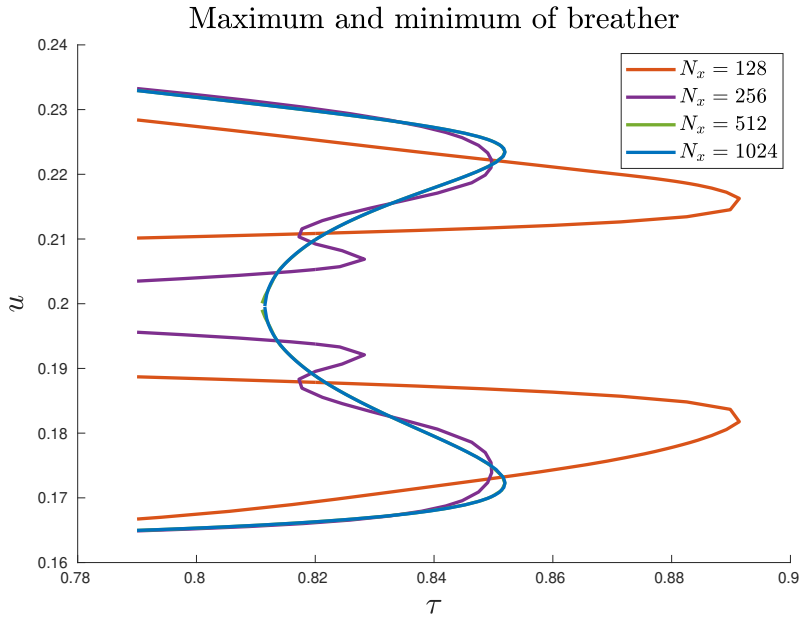

Figure 9: Convergence of numerical scheme for different values of N_x for the stationary breather. The curves have been continued with respect to τ, other parameters are as listed in Table 1.

blue saddle-node bifurcation curve of stationary breathers. Therefore, no stationary breathers exist below the dark blue fold curve of stationary breathers. The stability of the various patterns is calculated by calculating the eigenvalues of the Jacobian, introduced in section 3.7 and plotted in Figure 13.

At the top of Figure 10a areas with bistability are shown and these are highlighted in Figure 11. The areas with bistability have been observed and are shown in Figure 11. Two different bistable areas emerge. The left area consists of Stationary bumps and Travelling breathers. Traversing the drift bump curve we arrive at the right area where both travelling bumps and travelling breathers coexist.

The same parameter space has also been mapped for $\beta = 300$, this is shown in Figure 10b. Qualitatively the bifurcation diagrams of $\beta = 500$ and $\beta = 300$ are the same with some quantitative differences. The Hopf and fold curves of both stationary and travelling breathers move closer together is the most eye-catching difference between $\beta = 500$ and $\beta = 300$. These two curves moving together greatly limits the parameter region in which we can find stable stationary and travelling breathers.

In order to understand the connection between the bifurcation diagrams at $\beta = 500$ and $\beta = 300$, we scan the β–$\bar{w}_{ii}$ parameter space for $\tau = 0.90$ which is shown in Figure 12. Figure 12 clearly shows the Hopf curve from which the stationary and travelling breathers emerge undergo a generalised Hopf bifurcation at $\beta \approx 230$. This is consistent with the loss of stable breathers observed in Figure 10b with respect to Figure 10a. The Hopf curve of travelling breathers ends in a drift-Hopf bifurcation at $(\beta, \bar{w}_{ii}) = (107, 0.291)$. At this drift-Hopf bifurcation another drift curve of breathers emerges which ends in another drift-Hopf bifurcation at $(\beta, \bar{w}_{ii}) = (40, 0.366)$. The drift curve of bumps connects both areas of travelling bumps into one parameter region. Furthermore, a fold curve of stationary bumps has been found shown in dark red. At this curve, the stable bump solutions undergo a fold bifurcation, at which the stationary bumps destabilise into unstable stationary bumps.

To understand the stability of patterns in Figure 12, we have constructed an overview of the existence and stability of the patterns in the β–$\bar{w}_{ii}$ parameter space in Figure 14. Due to the instability of travelling breathers, the continuations fail for high values of $\bar{w}_{ii}$. Therefore, the region of unstable travelling breathers does not end at a bifurcation curve but at the $\bar{w}_{ii}$ value continuations failed to converge.

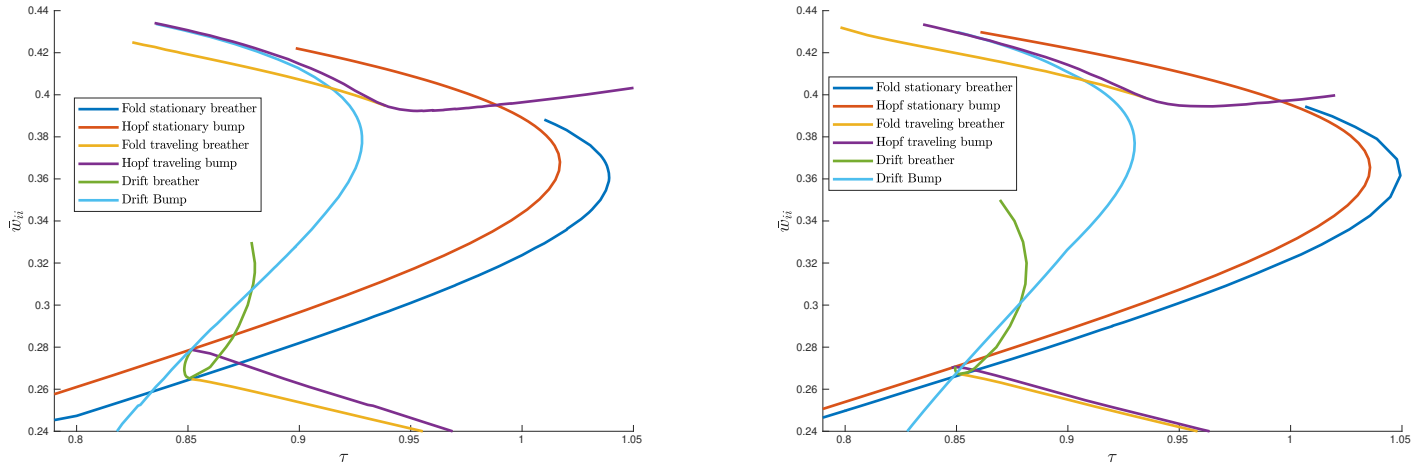

(a) $\beta = 500$ **(b)** $\beta = 300$

Figure 10: Bifurcation diagram in the τ–$\bar{w}_{ii}$ parameter space with (a) $\beta = 500$ and (b) $\beta = 300$. Other parameter values are as listed in Table 1.

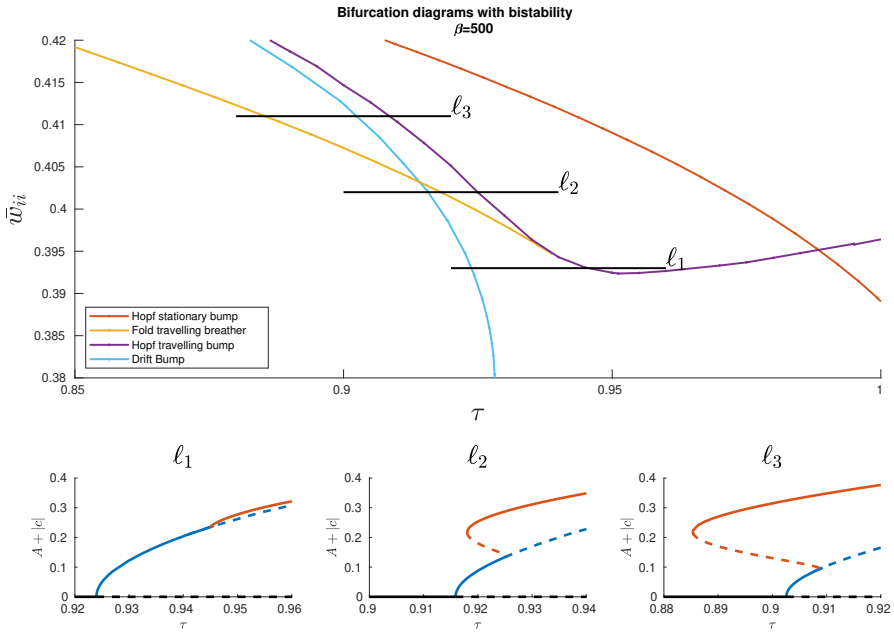

Figure 11: Bistability in Figure 10b. The top image shows a excerpt of Figure 10a where bistability exists. Continuation results have been plotted for each of the lines ℓ_i. The value of the amplitude of the breather A plus the wave speed c has been plotted to show the Hopf and drift bifurcations simultaneously.

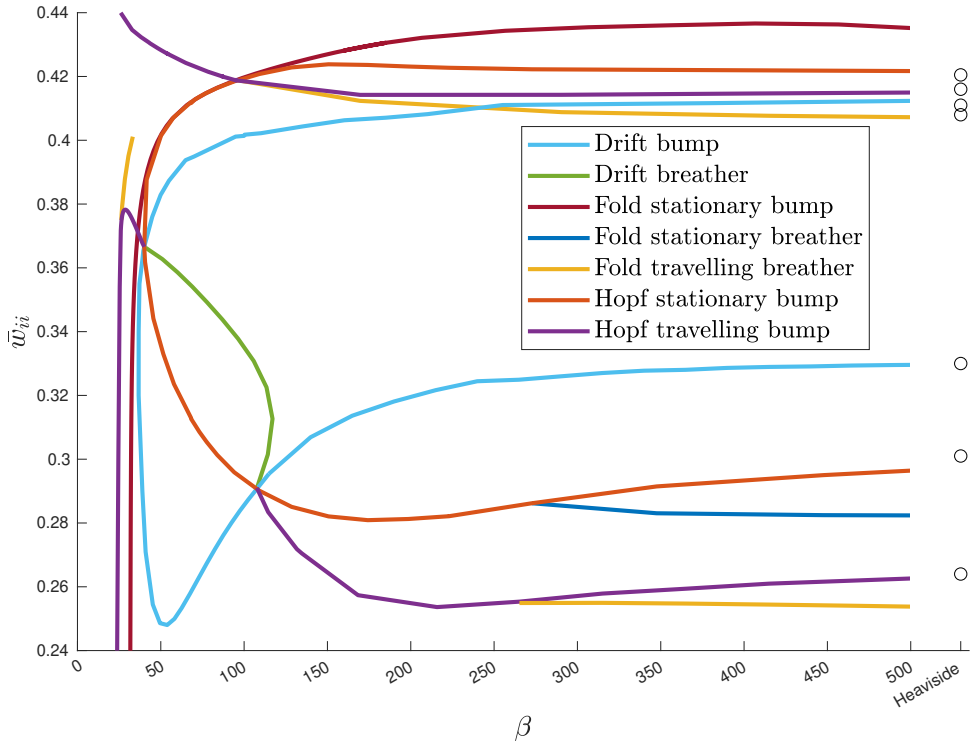

Figure 12: Bifurcation diagram in the β–$\bar{w}_{ii}$ parameter space with $\tau = 0.90$. Black circles coincide with the Heaviside limit [11]. Other parameter values are as listed in Table 1.

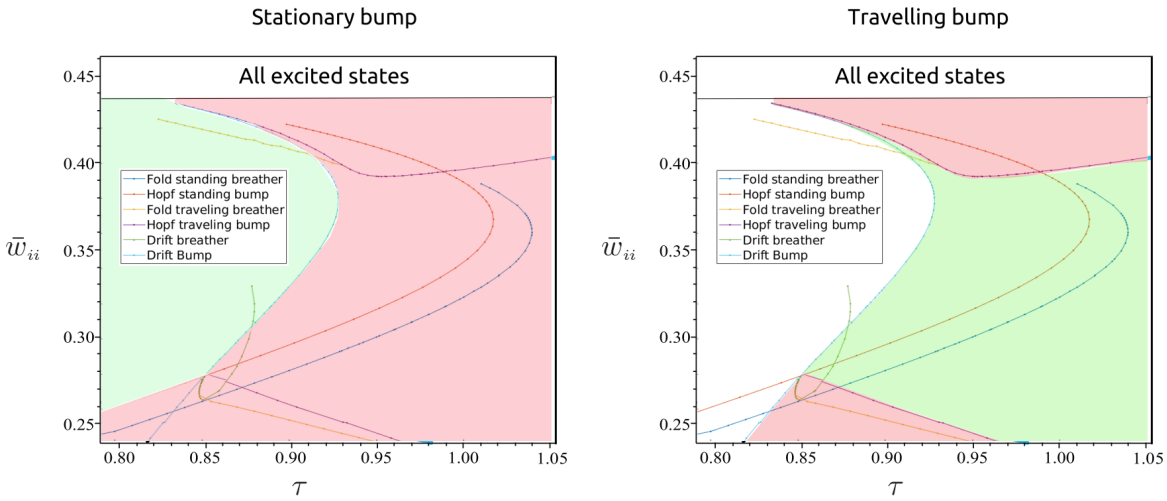

(a) Stationary bump

(b) Travelling bump

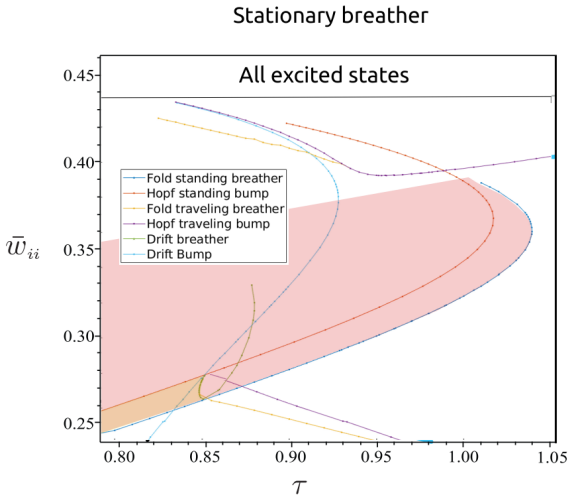

(c) Stationary breather

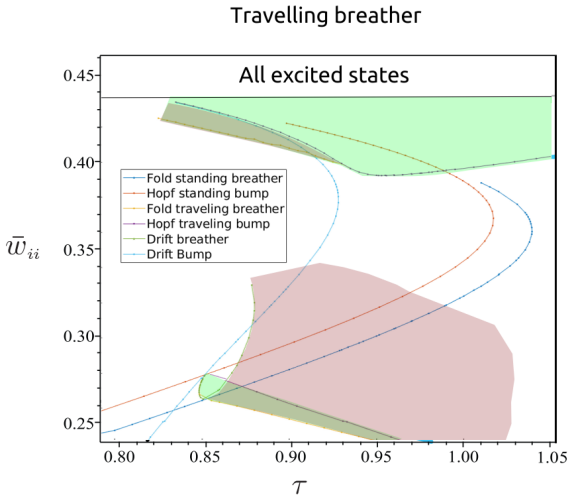

(d) Travelling breather

Figure 13: Stability of the patterns in the τ–$\bar{w}_{ii}$ parameter plane with other parameters as listed in Table 1. Green areas indicate the existence of stable patterns. Red areas indicate the existence of unstable patterns. Orange areas mark areas where both stable and unstable patterns exist. The existence of travelling patterns is shown only whenever $c > 0$ such that the graphs of standing and travelling patterns do not overlap.

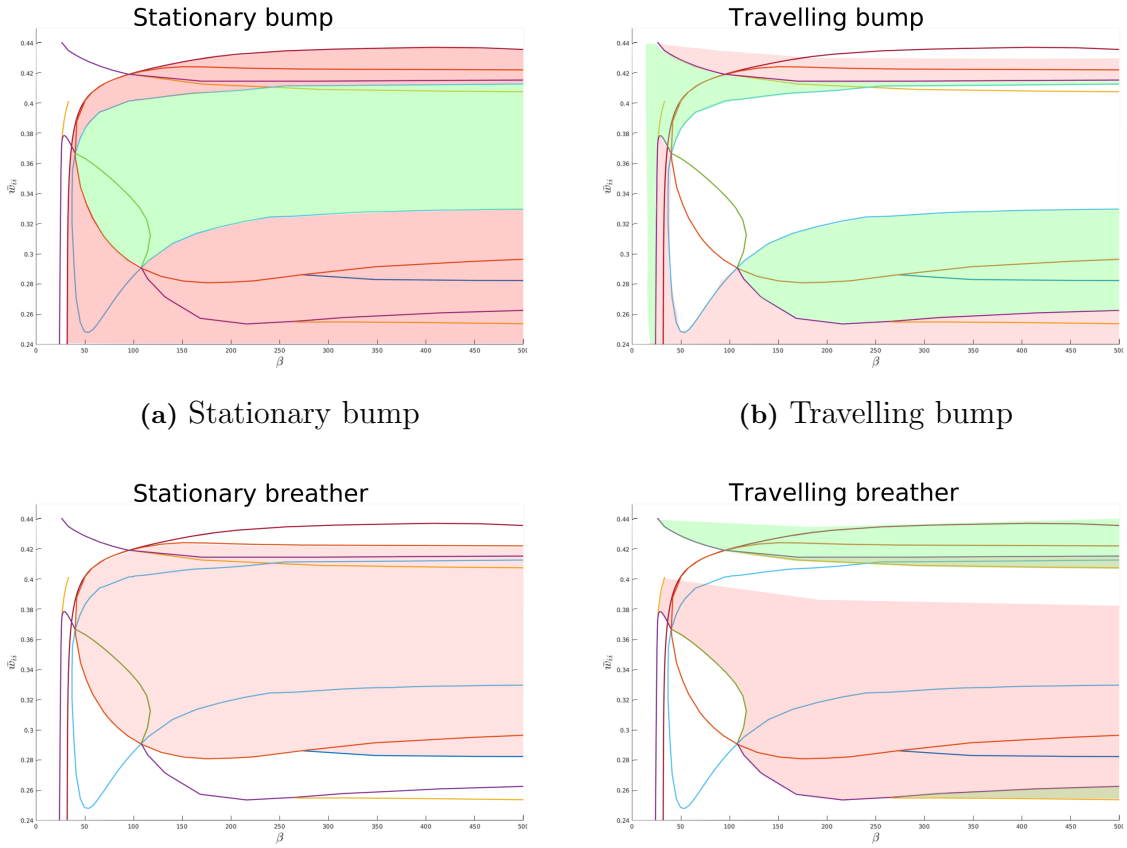

(a) Stationary bump

(b) Travelling bump

(c) Stationary breather

(d) Travelling breather

Figure 14: Stability of the patterns in the β–$\bar{w}_{ii}$ parameter plane with other parameters as listed in Table 1. Green areas indicate the existence of stable patterns. Red areas indicate the existence of unstable patterns. Orange areas mark areas where both stable and unstable patterns exist. The existence of travelling patterns is shown only whenever $c > 0$ such that the graphs of standing and travelling patterns do not overlap.

4.2 Adaptive neural field

The adaptive neural field (4) has been integrated resulting in three qualitatively different patterns which are shown in Figure 15. For $I_0 = 0.9$ a stationary bump solution is shown in the left of Figure 15. The middle figure shows a stationary breather solution with $I_0 = 1.9$. This stationary breather dies out completely between the maxima of the breather. Finally, the right figure shows a different stationary breather at $I_0 = 1.99$ where the breather has a much lower amplitude and oscillates around the bump solution.

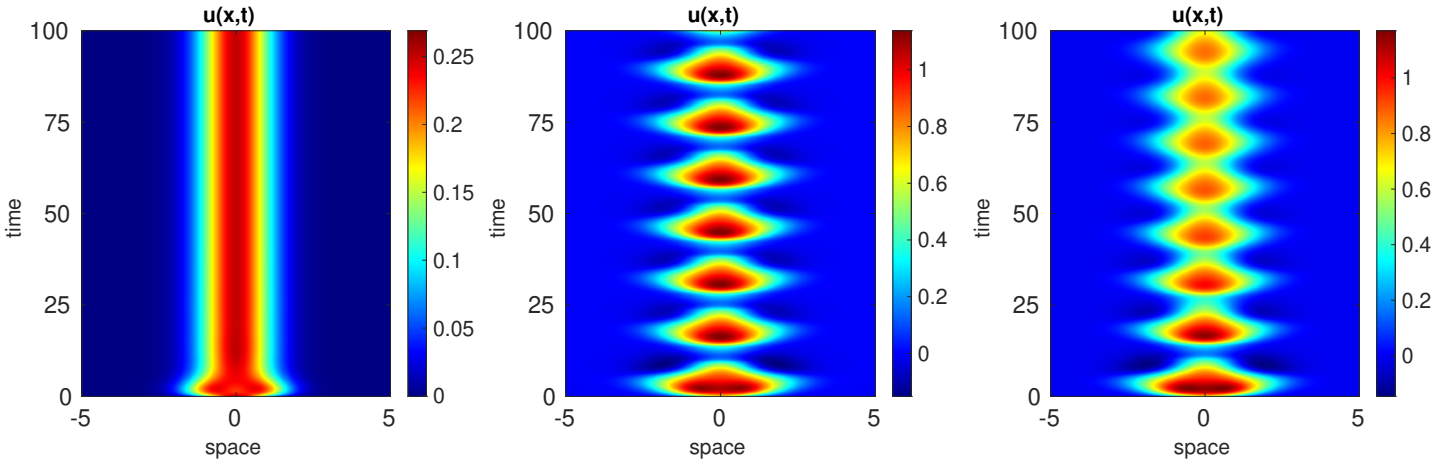

Figure 15: Integration results for different values of $I_0 = 0.9$ (left), $I_0 = 1.9$ (middle), and $I_0 = 1.99$ (right). Other parameters are as listed in Table 2.

To find the desired spatial discretisation we continue the stationary breather in the adaptive neural field (4) for different values of β and N_x. Figure 16 shows the calculated period throughout the continuation for $\beta = 20$, $\beta = 100$, and $\beta = 200$ against the external input I_0. The period has been plotted because it makes the differences between the discretisations most clear. Figure 16 makes it is clear that higher values of β require higher discretisations for accurate results in order to get consistent cointinuation results. Therefore, we use

$$N_x = \begin{cases} 256 & \beta < 20, \\ 512 & 20 < \beta < 100, \\ 1024 & \beta > 100. \end{cases}$$

In order to connect the different solutions in Figure 15 we construct the bifurcation

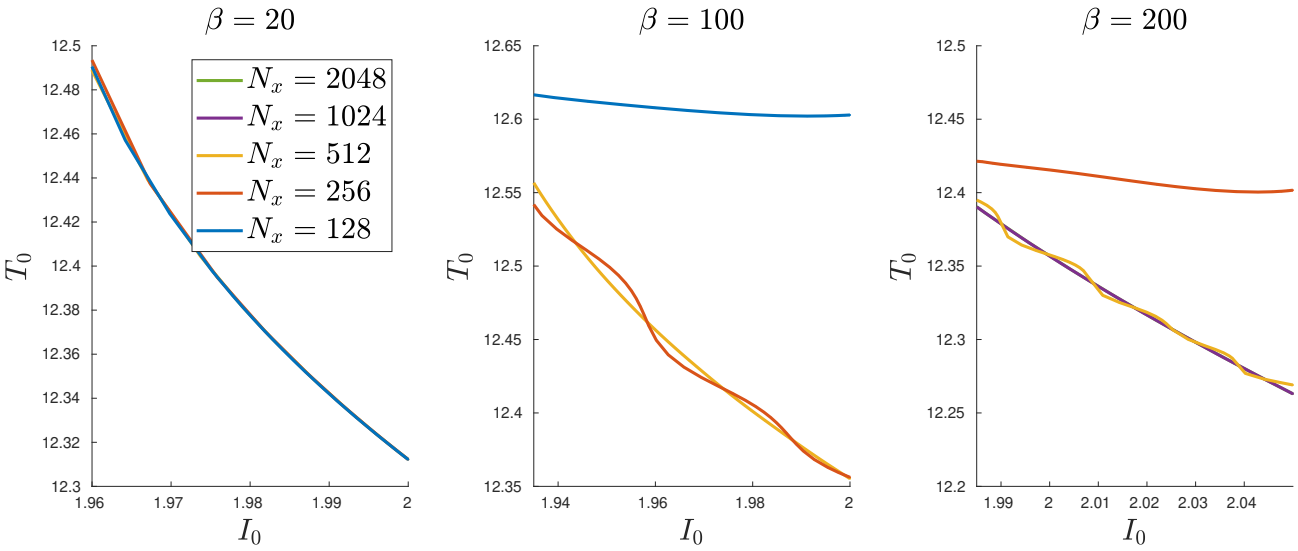

Figure 16: Convergence of the numerical scheme for different spatial discretisations at different values of β. Other parameters are as listed in Table 2.

diagram at $\beta = 20$ shown in Figure 17b. This figure shows a stationary bump solution that increases destabilizes through a supercritical Hopf bifurcation at $I_0 = 0.9946$. We follow the blue stationary breather, starting at this supercritical Hopf bifurcation. First, we encounter unstable breathers for $0.9521 \leq I_0 \leq 0.9946$. At $I_0 = 0.9521$ the unstable breather stabilizes through a saddle-node bifurcation. This high-amplitude breather encounters two more saddle-node bifurcations at $I_0 = 1.9856$ and $I_0 = 1.9530$. At this final saddle-node bifurcation, the breathers turn into the smaller amplitude breather shown in Figure 15(right). This branch of stationary breathers ends in a subcritical Hopf bifurcation of the stationary breather at $I_0 = 2.0478$ which stabilizes the stationary bump solution.

When we focus on higher values of β and set $\beta = 100$, we encounter a slightly more complex bifurcation diagram. The stationary breather curve is qualitatively the same as for $\beta = 20$. However, the stationary bump solution undergoes two fold bifurcations at $I_0 = 1.3124$ and $I_0 = 1.1649$, respectively. This does not change the stability of the stationary bump as it stays unstable.

Finally, we shift our focus on lower values of β and let $\beta = 6$. The stationary bump is qualitatively the same as for $\beta = 20$. The Hopf bifurcation for low I_0 has switched to a supercritical Hopf bifurcation. The emerging stationary bump solution does

not encounter saddle-node bifurcations and destabilizes through another supercritical Hopf bifurcation.

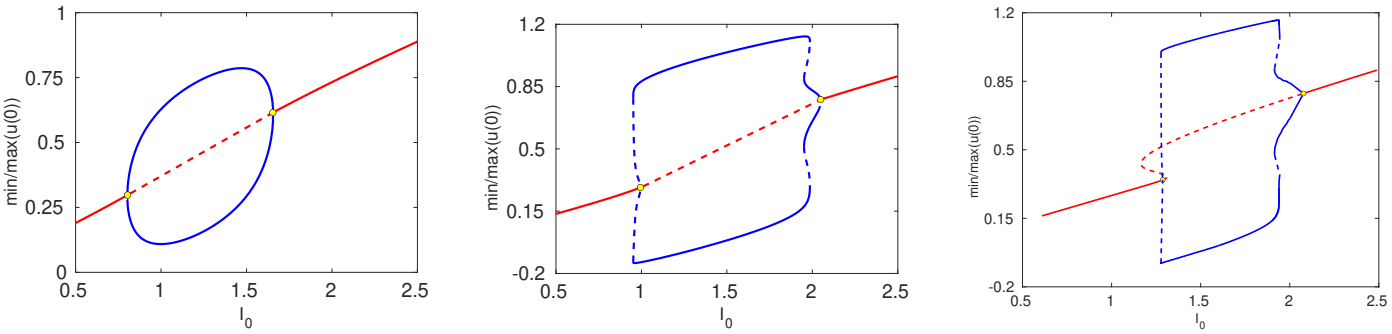

(a) $\beta = 6$ **(b)** $\beta = 20$ **(c)** $\beta = 100$

Figure 17: Amplitude at $x = 0$ for $\beta = 6$ (left), $\beta = 20$ (middle) and $\beta = 100$ (right). The stationary bump is indicated by the red curves and the stationary breather by the red curves. Solid and dashed lines represent stable and unstable solutions respectively.

In order to explain the qualitative differences between 17a, 17b, and 17c, we construct the bifurcation digram in the β–I_0 parameter plane. This bifurcation digram is shown in Figure 18. For $(\beta, I_0) = (29.5 \pm 0.5, 1.2005 \pm 0.0005)$, we observe a cusp bifurcation of stationary bump solutions from which two fold bifurcations of stationary bumps emerge. Another cusp bifurcation is observed at $(\beta, I_0) = (10.5 \pm 0.5, 1.947 \pm 0.005)$ at which two saddle-node bifurcations of stationary breathers emerge.

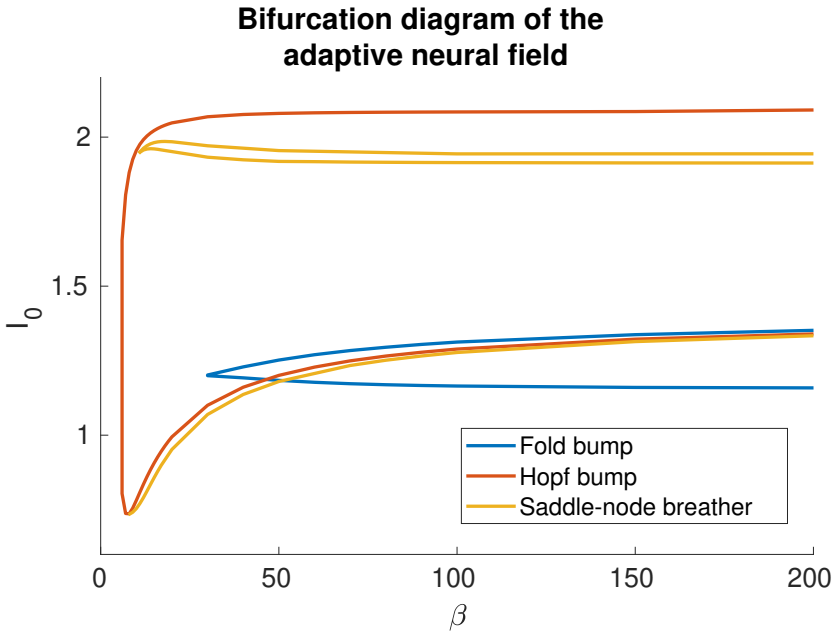

Figure 18: Bifurcation diagram of adaptive neural field (4) in the β–I_0 parameter plane. Red lines indicate the Hopf bifurcation of the stationary bump. Blue curves indicate fold bifurcations of the stationary bump solution. The yellow curves show saddle-node bifurcations of stationary breathers.

Parameter	Default value
$\bar{w}$	1
σ	1
σ_I	1.2
κ	2.75
τ	10
I_0	1.9
θ	0.375
β	20

Setting	Default value
N_x	128
Correction threshold	10^{-6}
GMRES maximum iterations	500
GMRES convergence threshold	10^{-10}
Time steps per section n	500
N_t	10
Continuation steps with pseudo-arclength continuation after failed natural continuation	3
Maximum step size h_{max}	0.05
Minimum step size h_{min}	10^{-6}

Table 2: Default values of parameters and continuation settings for continuation of the adaptive neural field (4).

5 Discussion

In this project, we set out to identify the effect of the slope parameter on the existence and stability of patterns in neural field models. Results have been obtained for two different models, an excitatory - inhibitory neural field model (1) [33] and an adaptive neural model (4) [21, 22].

5.1 Continuation schemes

We have implemented a continuation scheme based on secant predictions with adaptive step size to numerically continue stationary and travelling bumps and breathers in neural fields. To improve computation time, we have used matrix-free continuation methods based on GMRES to continue stationary patterns. The directional derivatives have been computed exactly. Stationary breathers have been continued using a multiple shooting approach to improve convergence along unstable branches. Travelling bumps and breathers have been continued in travelling wave coordinates using matrix-free continuation as well. However, due to the convection term in equation (41), convergence was worse compared to the stationary patterns. By employing scanning procedures, two-parameter bifurcation diagrams have been obtained. These bifurcation diagrams map the bifurcations in the τ–$\bar{w}_{ii}$ and β–$\bar{w}_{ii}$ parameter plane of neural field (1) and the β–I_0 parameter plane of neural field (4)

The continuations of neural field (1) have been run on a laptop with an i7-4710MQ processor with 16GB RAM running Ubuntu 20.04 LTS. One correction step for the stationary bump with $N_x = 512$ takes 416 milliseconds on average with 10 GMRES iterations, one correction for the travelling bump with $N_x = 512$, $N_t = 20$ takes 16.7 seconds with 200 GMRES iterations, one correction of the travelling bump with $N_x = 512$ takes 2.5 seconds, and one correction of the travelling breather with $N_x = 2048$ takes about 30 seconds. These runtimes are a big improvement over full matrix continuation constructed with finite differences where correction for the travelling breather with $N_x = 256$ and $N_T = 20$ takes about 30 minutes. Therefore, this is 100 times as slow as our implementation.

The number of GMRES iterations required for the stationary breather scaled with the number of sections N_t, requiring approximately ten iterations per section. On the other hand, increasing N_x has no significant influence on the number of GMRES iterations. Larger values of N_x increased the computation time of the numerical integration when calculating directional derivatives, increasing the computation time.

The limiting behaviour for larger values of the slope parameter shows convergence

towards the Heaviside limit. These results are the same as expected because the sigmoidal activation function converges in measure towards the Heaviside function. Due to the discontinuity of the Heaviside limit, we cannot use the numerical continuation method for large values of β; $f_h(u(x,t))$ does not change continuous and numerical continuation is not applicable.

Next to the stationary and periodic bumps and breathers, neural fields can exhibit sloshers [9]. Sloshers are asymmetric periodic solutions of the neural field. Although we have not implemented the continuation of sloshers, this could be performed by integrating over half the period and employing the asymetricity requiring $u(x,t_0) = u(-x,t_0+T_0)$.

5.2 Excitatory - inhibitory neural field model

The excitatory - inhibitory neural field model has been mapped in the τ–$\bar{w}_{ii}$ parameter plane for $\beta = 500$ and $\beta = 300$ in Figure 10a and 10b respectively. The bifurcation diagram with $\beta = 500$ corresponds with the numerical simulation results by Folias[11]. The bistable region and the proposed bifurcation diagrams [11] along the lines ℓ_i in Figure 11 have been confirmed by numerical continuation. Furthermore, the unstable stationary breathers have been continued to fully map the existence of stationary breathers in the τ–$\bar{w}_{ii}$ parameter space. In addition to the stable patterns, we found unstable stationary and travelling bumps and breathers in Figure 13. These continuations revealed a new fold bifurcation of stationary breathers. Here one eigenvalue of the monodromy matrix crosses the unit circle indicating a stability switch for breathers.

Comparing the bifurcation diagram of $\beta = 300$ with the bifurcation diagram of $\beta = 500$, we observe that the fold curve of stationary breathers and the Hopf curve of stationary bumps move closer together. Therefore, the parameter region in which stationary breather solutions exists is significantly smaller for $\beta = 300$. A similar change occurs for the lower branch of travelling breather solutions. Equivalent to the Hopf and fold curves for the stationary breather, the Hopf and fold curves for the lower branch of travelling breathers move closer together. Therefore, the parameter region in which stable travelling breathers exist shrinks significantly.

The β–$\bar{w}_{ii}$ bifurcation diagram shows us that unstable breathers exist for low values of β. Two more drift-Hopf bifurcations have been found for $\beta \approx 107$ and $\beta \approx 40$. These two bifurcations lie on the same stationary drift curve, and a drift curve of breathers connects them. Outside of the drift curve of bump solutions, travelling bump solutions exist. Therefore, we can find travelling bump solutions for β values at

which no stationary bumps exist. For a stationary bump to exist, the excitatory layer has to excite itself enough to cancel the inhibitory feedback. However, a travelling bump can exist; in the absence of inhibition, a travelling bump is excited by the excitatory layer first. Afterwards, the inhibition overcomes the excitatory input and the neural field dies out behind the wave, explaining the abundance of travelling bump solutions.

Two different drift-Hopf bifurcations have been observed in the β–$\bar{w}_{ii}$ parameter plane. This codimension-two bifurcation has been proposed by Folias [11] and shows up in our scanning results. The drift-Hopf bifurcation appears when a Hopf bifucation coincides with a drift bifurcation. At the drift-Hopf bifurcation two additional bifurcation curves are born: a drift curve of breathers and a Hopf curve of travelling bumps.

The large dependence on the steepness of the excitatory - inhibitory neural field should not surprise us by theoretical analysis by Veltz and Faugeras [29] which suggests that the bifurcation curves of patterns could be disconnected by opening up a transcritical bifurcation which could be closed by some parameter perturbation.

A sigmoidal activation function with a steepness of $\beta = 300$ is still fairly steep indicated in Figure 2. Therefore, the effect of the steepness parameter is very high for the excitatory - inhibitory neural field model.

5.3 Adaptive neural field model

The adaptive neural field model has been analysed in the β – I_0 parameter plane. For values of $\beta > 30$, the bifurcation diagram does not change qualitatively; the same patterns emerge. The exact parameter values of the Hopf, fold, and saddle-node bifurcations changes slightly. Stationary breathers do not change qualitatively for $\beta > 10$. For parameter values of the steepness parameter below $\beta = 10$, two saddle-node bifurcations disappear at the top of the diagram through a cusp bifurcation. The lower saddle-node bifurcation disappears through a generalised Hopf bifurcation around $\beta = 7.7$. Although the generic unfolding of the Hopf bifurcation along the curve has been analysed by Folias [10] the saddle-node bifurcations together with the generalised Hopf bifurcations are new.

The stationary breathers disappear for $\beta < 6$ where only stationary bump solutions remain. The activation function with $\beta = 6$ is shown in Figure 2 and is visually very shallow; whenever the activity of the neural field is zero, it would still excite itself.

5.4 Comparison

Comparing the results of the excitatory - inhibitory neural field model with the adaptive neural field model raises a difference. The excitatory - inhibitory neural field model exhibits significant changes for β as high as 250, the patterns in the adaptive neural field model change at significantly lower values of β. Moreover, in contrast to the excitatory - inhibitory neural field model, the stable stationary breathers became more abundant in the adaptive neural field model.

The continuation of stationary breathers did not perform similarly in both neural field models. The excitatory - inhibitory model has been more friendly towards the numerical continuation. This difference in performance was mainly due to the relatively small period $T_0 < 5$ for all breathers in this neural field. The continuation of stationary breathers in the adaptive model performed worse than in the excitatory - inhibitory model. The performance hit is due to the period changing $T_0 = 12$, all the way up to $T_0 = 30$ in some cases. These breathers with large periods are characterised by long intervals of inactivity. Continuation of these breathers is very expensive due to the evenly spaced sections.

6 Conclusion

In this research, we set out to find whether the results of the Heaviside analysis extend to neural fields with a sigmoidal activation function. We studied both stationary and travelling bumps and breathers in a 1D excitatory - inhibitory neural field model and a 1D adaptive neural field model. To investigate the existence and stability of these patterns we developed the required numerical continuation schemes.

The developed continuation schemes for the stationary bump, stationary breather, and travelling bump have desirable convergence behaviour. The continuation schemes can be used to efficiently calculate Hopf and fold bifurcation curves of stationary bumps, stationary breathers, and travelling bumps. Stability analysis of the travelling bump solutions can be used to calculate Hopf curves at which travelling breathers emerge. Because of convergence issues of GMRES, the developed continuation scheme for travelling breathers is a single shooting method. These convergence issues arise from the unbounded spectrum of the associated operator. Therefore, fold bifurcations of travelling breathers have been numerically expensive to locate. Convergence of the travelling breather continuation scheme could be improved by, for example, developing a suitable preconditioner.

The obtained β–$\bar{w}_{ii}$ and β–I_0 bifurcation diagrams converge for large values of β. The convergence of the bifurcation curves is expected and shows consistency in the obtained results. In the case of the excitatory - inhibitory neural field model, the curves converge approximately to the bifurcation values found by numerical simulations [11].

The two neural field models have shown different behaviour for lower values of the slope parameter β. The excitatory - inhibitory neural field model showed a relatively large dependence on the slope parameter; stable stationary and travelling breathers disappeared for $\beta < 250$. On the other hand, travelling bumps are abundant throughout the β–$\bar{w}_{ii}$ parameter plane as the travelling bumps do not disappear for low values of the slope parameter. The β–$\bar{w}_{ii}$ parameter space exhibits two co-dimension 2 Hopf-drift bifurcations. This bifurcation requires more in-depth research to explore, for example, its generic unfolding [6] that has not been described in the literature.

The adaptive neural field showed a different response to variations in the slope parameter compared to the excitatory - inhibitory neural field model. The β–I_0 bifurcation diagram does not change qualitatively for $\beta > 40$. The stationary breathers do not disappear until β is lower than 10. Finally, the stationary breathers disappear for $\beta < 6$.

Furthermore, we have not analysed the existence and stability of stationary sloshers. Analysing stationary sloshers should be possible by numerical continuation by employing $u(x, t_0) = u(-x, t_0 + T_0)$. Stability analysis of stationary sloshers may point towards the existence of travelling sloshers.

Obtained results have shown that the effect of the slope parameter is not the same for neural field models. Different neural field models have different responses to lower values of the slope parameter. Therefore, we cannot generally assume that the Heaviside analysis holds for neural tissue. To quantify the effect of the slope parameter on the existence and stability of patterns in neural fields, neural field models have to be analysed on a per-model basis using the numerical continuation schemes developed.

References

[1] S. I. Amari. Dynamics of pattern formation in lateral-inhibition type neural fields. *Biological Cybernetics*, 27(2):77–87, 1977.

[2] F. M. Atay and A. Hutt. Stability and bifurcations in neural fields with finite propagation speed and general connectivity. *SIAM Journal on Applied Mathematics*, 65(2):644–666, 2005.

[3] W. J. Beyn, A. Champneys, E. Doedel, W. Govaerts, Y. A. Kuznetsov, and B. Sandstede. Chapter 4 Numerical continuation, and computation of normal forms. *Handbook of Dynamical Systems*, 2:149–219, 2002.

[4] P. Blomquist, J. Wyller, and G. T. Einevoll. Localized activity patterns in two-population neuronal networks. *Physica D: Nonlinear Phenomena*, 206(3-4):180–212, 2005.

[5] P. C. Bressloff, S. E. Folias, A. Prat, and Y. X. Li. Oscillatory waves in inhomogeneous neural media. *Physical Review Letters*, 91(17):1–4, 2003.

[6] M. Brin and G. Stuck. *Introduction to Dynamical Systems*. Cambridge University press, 2002.

[7] S. Coombes, P. beim Graben, R. Potthast, and J. Wright. *Neural Fields*. 2014.

[8] A. Doelman. *Pattern formation in reaction-diffusion systems- an explicit approach*. 2019.

[9] G. Faye and J. Touboul. Pulsatile localized dynamics in delayed neural field equations in arbitrary dimension. *SIAM Journal on Applied Mathematics*, 74(5):1657–1690, 2014.

[10] S. E. Folias. Nonlinear analysis of breathing pulses in a synaptically coupled neural network. *SIAM Journal on Applied Dynamical Systems*, 10(2):744–787, 2011.

[11] S. E. Folias. Traveling waves and breathers in an excitatory-inhibitory neural field. *Physical Review E*, 95(3):1–16, 2017.

[12] S. E. Folias and P. C. Bressloff. Breathing pulses in an excitatory neural network. *SIAM Journal on Applied Dynamical Systems*, 3(3):378–407, 2004.

[13] A. Hutt and N. Rougier. Activity spread and breathers induced by finite transmission speeds in two-dimensional neural fields. *Physical Review E - Statistical, Nonlinear, and Soft Matter Physics*, 82(5):1–4, 2010.

[14] K. Kolodina, V. Kostrykin, and A. Oleynik. Existence and stability of periodic solutions in a neural field equation. *arXiv*, pages 1–22, 2017.

[15] Y. A. Kuznetsov. *Elements of Applied Bifurcation Theory*. Springer, Utrecht, 1994.

[16] H. G. Meijer and S. Coombes. Travelling waves in models of neural tissue: from localised structures to periodic waves. *EPJ Nonlinear Biomedical Physics*, 2(1):1–18, 2014.

[17] H. G. Meijer, F. Dercole, and B. Oldeman. Numerical Bifurcation Analysis. (2004):6329–6352, 2007.

[18] H. G. Meijer, T. L. Eissa, B. Kiewiet, J. F. Neuman, C. A. Schevon, R. G. Emerson, R. R. Goodman, G. M. McKhann, C. J. Marcuccilli, A. K. Tryba, J. D. Cowan, S. A. van Gils, and W. van Drongelen. Modeling focal epileptic activity in the Wilson-Cowan model with depolarization block. *Journal of Mathematical Neuroscience*, 5(1), 2015.

[19] L. Muller and A. Destexhe. Propagating waves in thalamus, cortex and the thalamocortical system: Experiments and models. *Journal of Physiology Paris*, 106(5-6):222–238, 2012.

[20] M. Net and J. Sánchez. Continuation of bifurcations of periodic orbits for large-scale systems. *SIAM Journal on Applied Dynamical Systems*, 14(2):674–698, 2015.

[21] D. J. Pinto and G. B. Ermentrout. Spatially Structured Activity in Synaptically Coupled Neuronal Networks : I . Traveling Fronts and Pulses. *SIAM Journal on Applied Mathematics*, 62(1):206–225, 2001.

[22] D. J. Pinto and G. B. Ermentrout. Spatially Structured Activity in Synaptically Coupled Neuronal Networks: II. Lateral Inhibition and Standing Pulses. *SIAM Journal on Applied Mathematics*, 62(1):206–225, 2001.

[23] W. H. Press, S. A. Teukolsky, W. T. Vetterling, and B. P. Flannery. *Numerical recipes—the art of scientific computing*, volume 71. 1986.

[24] J. Rankin, D. Avitabile, J. Baladron, G. Faye, and D. J. B. Lloyd. Continuation of Localized Coherent Structures in Nonlocal Neural Field Equations. *Society*, 18(3):1082–1105, 2007.

[25] K. A. Richardson, S. J. Schiff, and B. J. Gluckman. Control of traveling waves in the mammalian cortex. *Physical Review Letters*, 94(2):1–4, 2005.

[26] H. Schmidt and D. Avitabile. Bumps and oscillons in networks of spiking neurons. *Chaos*, 30(3), 2020.

[27] K. Takagaki, C. Zhang, J. Y. Wu, and M. T. Lippert. Crossmodal propagation of sensory-evoked and spontaneous activity in the rat neocortex. *Neuroscience Letters*, 431(3):191–196, 2008.

[28] J. S. Umbría and M. Net. Numerical continuation methods for large-scale dissipative dynamical systems. *European Physical Journal: Special Topics*, 225(13-14):2465–2486, 2016.

[29] R. Veltz and O. Faugeras. Local/global analysis of the stationary solutions of some neural field equations. *SIAM Journal on Applied Dynamical Systems*, 9(3):954–998, 2010.

[30] N. A. Venkov, S. Coombes, and P. C. Matthews. Dynamic instabilities in scalar neural field equations with space-dependent delays. *Physica D: Nonlinear Phenomena*, 232(1):1–15, 2007.

[31] I. Waugh, S. Illingworth, and M. Juniper. Matrix-free continuation of limit cycles for bifurcation analysis of large thermoacoustic systems. *Journal of Computational Physics*, 240:225–247, 2013.

[32] H. R. Wilson and J. D. Cowan. Excitatory and Inhibitory Interactions in Localized Populations of Model Neurons. *Biophysical Journal*, 12(1):1–24, 1972.

[33] H. R. Wilson and J. D. Cowan. A mathematical theory of the functional dynamics of cortical and thalamic nervous tissue. *Kybernetik*, 13(2):55–80, 1973.

[34] J. Y. Wu, L. Guan, and Y. Tsau. Propagating activation during oscillations and evoked responses in neocortical slices. *Journal of Neuroscience*, 19(12):5005–5015, 1999.

[35] Z. Yang, D. J. Heeger, R. Blake, and E. Seidemann. Long-range traveling waves of activity triggered by local dichoptic stimulation in V1 of behaving monkeys. *Journal of Neurophysiology*, 113(1):277–294, 2015.

A Numerical Evans function

During the derivation of the Evans function in section 2.4.2 we have used the Dirac delta function as the derivative of the activation function which we have used to simplify equation (12) to the local evaluation of φ_k at ξ_n^k. However, for a sigmoidal activation function equation (12) does not simplify as before.

In case of the sigmoidal firing rate function, the derivative f_k' does have support on $\mathbb{R}$. However, for $\left|x - \xi_n^k\right| > 0$ the value of $f_k'(u_k(x))$ decays exponentially and we can approximate f_k' with zero whenever $f_k'(x)$ is smaller than some threshold variable θ_{zero}. This allows us to reduce equation (12) to

$$\mathcal{N}_{jk}\varphi_k = \int_{A_{jk}} w_{jk}(x-y) f_k'(u_k(y,t))\varphi_k(y)dy \tag{69}$$

where $A_{jk} = \{x | f_k'(u_k(x)) > \theta_{zero}\}$, figure 19 shows the situation schematically.

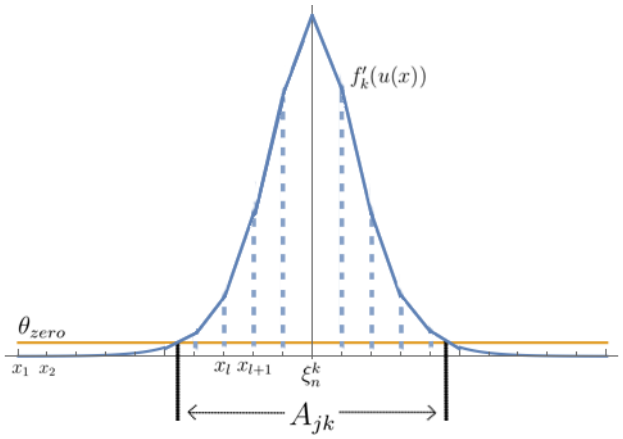

Figure 19: Schematic representation of the numerical approximation of $f_k'(u_k(x))$ around the threshold values ξ_n^k. Dashes on the x axis represent the grid points $\{x_l\}$, θ_{zero} is the numerical threshold below which we approximate $f_k'(u_k(x))$ by zero.

This integral can be approximated using the numerical approximation of $u_k(x)$ calculated to arrive at

$$\mathcal{N}_{jk}\varphi_k \approx \sum_{l=1}^{N} w_{jk}(x-x_l) f_k'(u_k(x_l,t))\varphi_k(x_l)\Delta x. \tag{70}$$

This approximation expands equation (15) to get a matrix equation

$$M(\lambda)\boldsymbol{\psi} = \boldsymbol{F} \tag{71}$$

with

$$M(\lambda) = \begin{bmatrix} -(1+\lambda)I + M_{ee} & -M_{ei} \\ M_{ie} & -(1+\tau\lambda)I - M_{ii} \end{bmatrix} \tag{72}$$

where I is the identity matrix of appropriate size and the matrix elements of M_{jk} at (l, m) are given by

$$M_{jk,(l,m)} = w_{jk}(x_m - x_l)f'(x_k(u(x_m^k))). \tag{73}$$

Therefore, equation (71) is singular whenever equation (11) has a nontrivial solution. Due to the scaling of the determinant for large matrices M, evaluating the determinant will not be feasible whenever M is too large. Instead, we find λ and v for which $M(\lambda)v = 0$ by Newton iterations. Given an initial guess (v^0, λ^0)

$$\begin{bmatrix} v^{i+1} \\ \lambda^{i+1} \end{bmatrix} = \begin{bmatrix} v^i \\ \lambda^i \end{bmatrix} + DF^{-1}(v^i, \lambda^i)F(v^i, \lambda^i) \tag{74}$$

where

$$F(v^i, \lambda^i) = \begin{bmatrix} A(\lambda)v \\ v^T v \end{bmatrix} \tag{75}$$

and

$$DF(v^i, \lambda^i) = \begin{bmatrix} A(\lambda) & A'(\lambda)v \\ 2v^T & 0 \end{bmatrix} \tag{76}$$

In the context of continuation, $\begin{bmatrix} v^0 \\ \lambda^0 \end{bmatrix}$ could be the converged value at the previous computed point on the curve.